Preferential Mode of gas invasion in sediments: Grain-scale mechanistic model of coupled multiphase fluid flow and sediment mechanics

A. K. Jain[1] and R. Juanes[1]

[1]   We present a discrete element model for simulating, at the grain scale, gas migration in brine-saturated deformable media. We rigorously account for the presence of two fluids in the pore space by incorporating forces on grains due to pore fluid pressures and surface tension between fluids. This model, which couples multiphase fluid flow with sediment mechanics, permits investigation of the upward migration of gas through a brine-filled sediment column. We elucidate the ways in which gas migration may take place: (1) by capillary invasion in a rigid-like medium and (2) by initiation and propagation of a fracture. We find that grain size is the main factor controlling the mode of gas transport in the sediment, and we show that coarse-grain sediments favor capillary invasion, whereas fracturing dominates in fine-grain media. The results have important implications for understanding vent sites and pockmarks in the ocean floor, deep subseabed storage of carbon dioxide, and gas hydrate accumulations in ocean sediments and permafrost regions. Our results predict that in fine sediments, hydrate will likely form in veins following a fracture network pattern, and the hydrate concentration will likely be quite low. In coarse sediments, the buoyant methane gas is likely to invade the pore space more uniformly, in a process akin to invasion percolation, and the overall pore occupancy is likely to be much higher than for a fracture-dominated regime. These implications are consistent with laboratory experiments and field observations of methane hydrates in natural systems.

1.   Introduction

[2]   Gas migration through water-filled soft sediment is an essential component of seafloor dynamics. It governs, for instance, the spatiotemporal characteristics of natural gas seeps and vent sites [*Judd et al.*, 2002; *Heeschen et al.*, 2003; *Best et al.*, 2006], the biochemical processes in the shallow subseafloor as well as the ocean floor [*Suess et al.*, 1999], the mechanical and acoustic properties of submarine sediments [*Anderson and Hampton*, 1980; *Anderson et al.*, 1998; *Waite et al.*, 2008], the creation of pockmarks in the ocean floor [*Hovland et al.*, 2002; *Sahling et al.*, 2008], and the accumulation of gas hydrate (notably methane) in ocean sediments. Understanding gas transport in soft sediments is also key to assessing the viability of carbon dioxide sequestration in the subseafloor, either by hydrate formation [*Koide et al.*, 1995, 1997b] or gravitational trapping [*Koide et al.*, 1997a; *House et al.*, 2006; *Levine et al.*, 2007; *Goldberg et al.*, 2008].

[3]   Methane hydrates (crystalline ice-like compounds composed of methane molecules caged in a lattice of water molecules [*Sloan*, 1998]) form naturally at high pressures and low temperatures, like those typical of most of the ocean floor. It is believed that an enormous pool of carbon exists in the form of methane gas and methane hydrate in oceanic sediment along the continental margins [*Kvenvolden*, 1988; *Sloan*, 2003], although the global estimates of the energy resource are highly uncertain. It also seems likely that this carbon pool plays an important role in massive submarine landslides [*Paull et al.*, 2003] and in the global carbon cycle [*Dickens*, 2003]; its sudden or gradual release has been hypothesized to be the cause of past and future climate change [*Dickens et al.*, 1995; *Buffett and Archer*, 2004; *Archer et al.*, 2009].

[4]   Methane hydrate systems in ocean sediments have been the subject of intense research in recent years. A significant component of that effort is directed toward gaining a better conceptual picture of the hydrogeological environment of gas hydrate systems. Particular attention has been devoted to the two end-members [*Trehu et al.*, 2006b]: (1) The hydrogeologically more active, dynamic end-member, exemplified by Hydrate Ridge, offshore Oregon [*Suess et al.*, 1999; *Tryon et al.*, 2002; *Heeschen et al.*, 2003; *Trehu et al.*, 2004b; *Weinberger et al.*, 2005] and

---

[1]Department of Civil and Environmental Engineering, Massachusetts Institute of Technology, Cambridge, Massachusetts, USA.
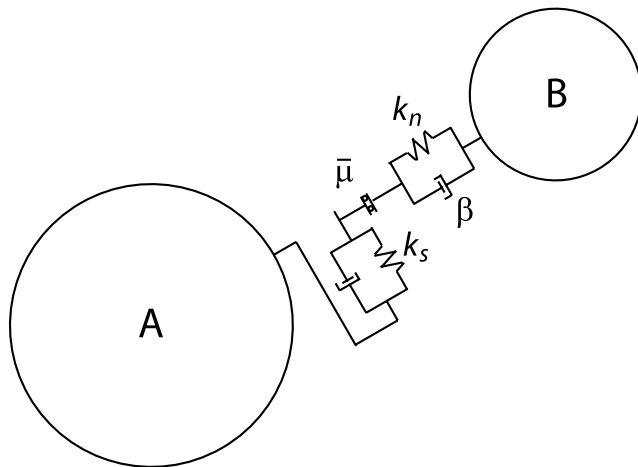
Figure 1. Schematic diagram of a grain-grain contact in a discrete element model. Elastic forces are represented by springs, with normal stiffness k_n and shear stiffness k_s. The contact model includes inelastic and irreversible mechanics through friction (a slider with friction coefficient $\bar{\mu}$), viscous damping (dashpots with damping coefficient β), and bond rupture.

(2) the hydrogeologically less active, quiescent end-member, illustrated by Blake Ridge, offshore South Carolina [*Holbrook et al.*, 1996; *Dickens et al.*, 1997; *Hornbach et al.*, 2007].

[5] One of the fundamental observations at these two sites is the coexistence of methane hydrate, gas and brine within the hydrate stability zone (HSZ). This is especially noticeable in dynamic environments [*Wood et al.*, 2002; *Milkov et al.*, 2004; *Torres et al.*, 2004; *Zühlsdorff and Spiess*, 2004; *Heeschen et al.*, 2007; *Sahling et al.*, 2008], but has been observed in low-flux hydrate provinces [*Gorman et al.*, 2002]. It seems clear that in some geologic settings, methane transport through the HSZ cannot occur solely as diffusive and advective transport of dissolved methane in the aqueous phase [*Torres et al.*, 2004; *Trehu et al.*, 2004a; *Liu and Flemings*, 2006].

[6] The scientific community is now undergoing a heated debate as to what are the reasons for coexistence of hydrate and gas [*Milkov and Xu*, 2005; *Torres et al.*, 2005; *Ruppel et al.*, 2005], which include (1) kinetics of hydrate formation [*Torres et al.*, 2004]; (2) regional geotherms [*Wood et al.*, 2002]; (3) hypersaline brines as a result of hydrate formation [*Milkov et al.*, 2004]; and (4) fast, focused flow of free gas through fractures and high-permeability conduits [*Flemings et al.*, 2003; *Hornbach et al.*, 2004]. The importance of methane migration as a separate gas phase, and the need to account for multiphase flow effects coupled with hydrate formation, have already been pointed out over a decade ago [*Ginsburg and Soloviev*, 1997; *Soloviev and Ginsburg*, 1997].

[7] It has been proposed that free gas accumulation beneath the HSZ may reach a critical thickness to dilate fractures or activate preexisting faults that will serve as conduits for fast upward gas migration [*Wood et al.*, 2002; *Flemings et al.*, 2003; *Trehu et al.*, 2004a; *Hornbach et al.*,

2004; *Zühlsdorff and Spiess*, 2004; *Obzhirov et al.*, 2004; *Netzeband et al.*, 2005; *Weinberger and Brown*, 2006; *Liu and Flemings*, 2006, 2007]. Although they did not address the problem at the grain scale, *Liu and Flemings* [2007] also predicted that at fine grain size and high capillary entry pressure, fracture propagation would dominate the process as gas pressure exceeded the horizontal stress. In this case, it is clear that the study of the hydrate system must be coupled with the mechanical response of the host sediments containing hydrate.

[8] Our hypothesis is that coupling of multiphase fluid flow and sediment mechanics leads, under certain conditions to be described below, to preferential fracturing of the sediment. The creation of these capillary pressure-driven fractures provides fast paths for upward migration of methane gas through the HSZ, which in turn explains the coexistence of methane gas and hydrate [*Behseresht et al.*, 2008; *Jain and Juanes*, 2008].

[9] In this paper, we support this hypothesis by developing a mechanistic model at the grain scale. We develop a discrete element method (DEM) to model the strong coupling between the pore fluids and the mechanical behavior of the sediment. We rigorously account for the presence of one or more fluids in the pore space by incorporating additional sets of forces due to pore fluid pressures and interfacial tension between the fluids. We demonstrate the DEM's ability to reproduce core-scale behavior, as measured by triaxial laboratory experiments and fluid flow tests. The proposed methodology elucidates the depositional environments (grain size and earth stresses) under which migration of methane gas by fracturing of the sediment is favored over capillary invasion. This determines the distribution of methane gas and hydrate, and the likelihood that gas and hydrate will coexist. Even though the analysis is done at the grain scale, these results have important implications at the geologic or planetary scale, such as for estimating the magnitude of methane fluxes into the ocean, and the overall size of the hydrate energy resource.

2. Theory, Formulation, and Methods

[10] The discrete element method (DEM) [*Cundall and Strack*, 1979] has proved a valuable tool to study the mechanisms for deformation and failure of granular materials with variable degree of cementation [*Bruno and Nelson*, 1991]. Moreover, based on simple geometric arguments, stress variations (and subsequent deformation) have been shown to affect flow properties such as porosity and permeability [*Bruno*, 1994].

[11] Each element or grain is identified separately by its own mass, moment of inertia and contact properties. For each grain, its translational and rotational movements are described by solving Newton's second law of motion. The mechanical behavior at the deformation region of each grain contact is approximated by introducing a grain contact model, such as a system of a spring, dashpot and slider (Figure 1).

2.1. Micromechanics of "Dry" Media

[12] The movement of a grain is dictated by the net force and moment acting on it. For a dry model, that is, one in which pore pressures are negligible, the forces for each
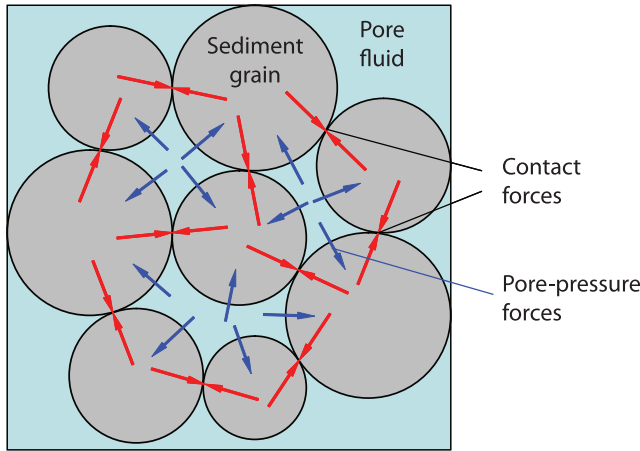
Figure 2. Conceptual picture of the fluid-solid interaction model at the pore scale when a single fluid is present.

grain may include (1) a contact force $\mathbf{F}_c$ due to deformation at the grain contacts, (2) a damping force $\mathbf{F}_d$ due to grain nonelastic collisions; and (3) an external force $\mathbf{F}_b$ due to gravity and prescribed tractions at the boundaries. The contact force $\mathbf{F}_c$ can be further split into normal and tangential components, $\mathbf{F}_c^n$ and $\mathbf{F}_c^s$, respectively.

[13] The simplest (linear elastic) mechanical behavior at the grain contacts is described by

$$F^n = k_n U_n, \quad \Delta F^s = -k_s \Delta U_s, \tag{1}$$

where U_n is the overlap, ΔU_s is the tangential displacement, and k_n and k_s are the normal and shear stiffness at the contact, respectively [Itasca Consulting Group, Inc. (Itasca), 2004; Potyondy and Cundall, 2004]. Inelastic behavior emerges due to either slip between grains, or breakage of contact bonds. Inelasticity is reflected by the constraints

$$F^s \leq \overline{\mu} F^n, \quad F^n \leq \varphi_n, \quad F^s \leq \varphi_s, \tag{2}$$

where $\overline{\mu}$ is the contact friction coefficient and φ_n and φ_s are the normal and shear strengths (in force units) of the contact.

[14] Bulk behavior of a granular system is a collective response determined by all the individual grain-grain interactions. For dry sample analyses, the interparticle interactions can be associated with a network of grain-grain contact forces connecting the centroids of grains that are in contact.

[15] Given the set of forces $\mathbf{F}_j$ and moments $\mathbf{M}_j$ acting on the ith particle, its motion is described by the following:

$$m_i \ddot{\mathbf{x}}_i = \sum_j \mathbf{F}_j \tag{3}$$

$$\mathbf{I}_i \ddot{\boldsymbol{\theta}}_i = \sum_j \mathbf{M}_j. \tag{4}$$

Here, $\mathbf{x}_i$ and $\boldsymbol{\theta}_i$ are the position vector of the grain centroid and the angle vector of rotation about the centroid; the double dots denote second time derivatives of the position and rotation angle; m_i is the mass; and $\mathbf{I}_i$ is the tensor of

moments of inertia, respectively. The equations of motion (3)–(4) must be solved simultaneously for all grains in the system via a numerical integration scheme. A commercial three-dimensional DEM code, PFC2D [Itasca, 2004], was used to integrate these equations in time.

2.1.1. Micromechanical Versus Macroscopic Parameters

[16] The parameters that need to be defined at the grain-scale level are ρ_s (grain density), $\overline{\mu}$, k_n, k_s, φ_n and φ_s, as well as the grain size distribution, which we shall characterize simply by the grain radius interval $r_{\min} \leq r_g \leq r_{\max}$.

[17] From DEM simulations of biaxial tests, the linear elastic macroscopic parameters (Young modulus E and Poisson ratio ν), as well as strength properties (yield stress σ_y, friction angle φ, cohesion c, etc.) may be computed. In order to obtain macroscopic parameters that are independent (or only slightly dependent) on the grain size, the contact strengths must scale with the grain size [Potyondy and Cundall, 2004]:

$$\varphi_n = \overline{\sigma}_c 2 r_g w, \quad \varphi_s = \overline{\tau}_c 2 r_g w, \tag{5}$$

where $\overline{\sigma}_c$ and $\overline{\tau}_c$ are the normal and shear contact strengths (in stress units), assumed to be independent of grain size, and w is the width of the 2-D assembly in the third dimension.

2.1.2. Time Step Selection for Mechanics Simulation

[18] Since explicit time integration is used, the time step is bounded by stability considerations. The characteristic time required to capture the dynamics is [Itasca, 2004]

$$\delta t \sim \sqrt{m/k_n}, \tag{6}$$

where m is the mass of the particle. In PFC2D, grains are assumed to be disks of unit width ($w = 1$ m), so $m = 2\pi r_g^2 w \rho_s$ and, therefore, the critical time step for mechanical stability scales as follows:

$$\delta t_{\mathrm{crit}}^{\mathrm{m}} \sim r_g \sqrt{\rho_s/k_n}. \tag{7}$$

2.2. Microporomechanics of Single-Fluid Systems

[19] From the theory of poromechanics [Biot, 1941], it is well known that pore pressure will influence mechanical behavior. Essentially, compressive stresses in granular media are transmitted both through a solid skeleton and the pore fluids. Recently, models have been developed to incorporate this effect in DEM with a single-phase pore fluid [Shimizu, 2004; Cook et al., 2004; Li and Holt, 2001, 2004].

[20] When the pore space is filled with a single fluid phase at nonnegligible pressure, the associated forces must be incorporated in the model. A conceptual view of the new set of forces is shown in Figure 2. Computationally, the model then consists of two overlapping and interacting networks: the grain network and the fluid network. A particular instance is shown in Figure 3. The force fluid in a given domain exerts on a neighboring grain is obtained by integrating the pressure along the pore-grain contact area. In our implementation, a pressure force is directed
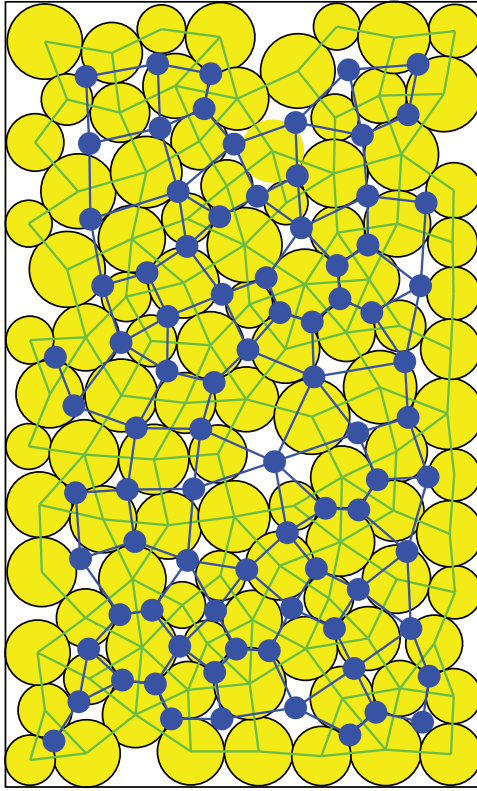
Figure 3. Representation of the grain assembly (yellow circles) and the grain network (green lines). At the center of each fluid domain is a pore body (blue dots), connected by the fluid network (blue lines).

from the center of the fluid domain to the grain center. Therefore, pressure forces do not induce rotation.

[21] Consider one particular fluid domain, as sketched in Figure 4. The micromechanical equations can be summarized as follows. The flow rate out of the fluid domain through a pore throat is

$$q_j = C_j \frac{p - p_j}{L_j}, \qquad (8)$$

where C_j is the throat conductance, L_j is an effective distance between pore centers, and p, p_j represent the pressures in the fluid domain and its neighbor, respectively. The conductance is inversely proportional to the fluid viscosity μ, and proportional to the square of the effective throat area A_j:

$$C_j = \frac{\tilde{C}_j}{\mu} \frac{A_j^2}{2r_g} w, \qquad (9)$$

where $\tilde{C}_j$ is a dimensionless throat conductance. The derivation of this equation from the solution of a Stokes flow problem, and the expressions for $\tilde{C}$ and A, are given in Appendix A.

[22] The grains have a certain compressibility, and the radius of a spherical grain varies according to

$$r_g = r_{g,0} \left(1 - \frac{p}{3K_s} \right), \qquad (10)$$

where $r_{g,0}$ is the initial radius (at zero fluid pressure), K_s is the bulk modulus of the solid grain, and p is the average of the pore pressures around the grain. Finally, mass balance over a fluid domain gives the following pressure evolution equation for a pore volume V_p:

$$\delta p = \frac{K_f}{V_p} \left(-\delta V_p - \sum_j q_j \delta t \right), \qquad (11)$$

where K_f is the fluid bulk modulus, and δp is the pressure variation after a time step δt. The main feature of our model is the term $-\delta V_p$, which accounts for the change in volume of each pore caused by changes in grain locations. This term has been neglected in previous investigations of pore-scale poromechanical models but is essential, for example, to reproduce pressurization of the fluid upon fast compaction. It also reflects the reverse coupling present in Biot's self-consistent theory of poroelasticity.

[23] There is a formal analogy between the microporomechanical equations (8)–(11) and Biot's self-consistent theory of poroelasticity [*Biot*, 1941; *Wang*, 2000]. We expect the DEM formulation will reproduce the linear theory of poroelasticity only in the range of small deformations and small pressure changes. Under such conditions, the poroelastic parameters can then be determined from DEM simulations. When these conditions are not met, nonlinear/irreversible behavior is expected to emerge in the DEM model, driven by contact slip, bond breaking and grain rearrangement.

2.2.1. Time Step Selection for Fluid Flow Simulation

[24] The grain-scale fluid flow equations (11) are solved using an explicit time integration scheme. The time step must be restricted for the scheme to be stable. The charac-
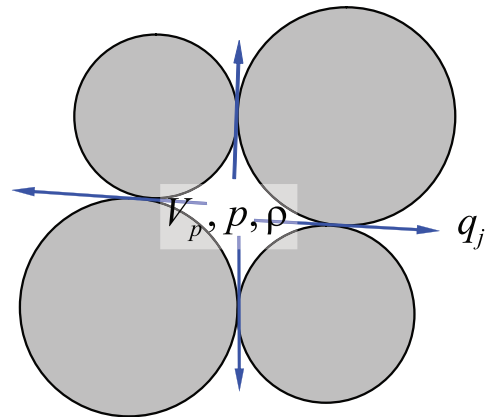
Figure 4. Schematic representation of a fluid domain. At any given time, each fluid domain is characterized by its pore volume V_p, and the pressure p and density ρ of the fluid. Fluid can go in and out of the pore domain at a rate q_j into the neighboring fluid domains.

teristic time associated with the microscopic fluid flow dynamics is

$$\delta t \sim \frac{V_p}{K_f} \frac{\delta p}{\sum_j q_j}. \tag{12}$$

Introducing equations (8) and (9), we express the characteristic time as

$$\delta t \sim \frac{V_p}{K_f} \frac{2 r_g \mu}{w} \sum_j \frac{L_j}{\bar{C}_j A_j^2}. \tag{13}$$

Using the scaling $V_p \sim r_g^2 w$, and $A \sim r_g^2$, the critical time step for fluid flow stability scales as follows:

$$\delta t_{\mathrm{crit}}^{\mathrm{f}} \sim \frac{\mu}{\bar{C} K_f}. \tag{14}$$

In a coupled poromechanics simulation, the time step must be smaller than the minimum of the critical values in equations (7) and (14).

### 2.3. Microporomechanics of Two-Fluid Systems

[25] In the environments of interest for methane hydrates, in particular, at the base of the hydrate stability zone, two fluid phases exist: a liquid brine phase, and methane gas. A key difference between single-fluid and two-fluid systems is the presence of a fluid-fluid interface. Because of surface tension effects, the pressures on either side of the interface (that is, the pressure in the brine and the pressure in the methane gas) can be very different.

[26] The key question is: what is the preferential mode of gas invasion? Two different fundamental mechanisms are at play (Figure 5): (1) capillary-dominated invasion of a rigid solid skeleton, and (2) fracturing of the sediment. While capillarity governs invasion of gas through the porous medium, mechanical effects may lead to deformation and fracturing of the sediment skeleton, thereby triggering invasion when it would otherwise not occur. Preferential fracturing of the sediment requires differences in pressure between neighboring pores. While this is
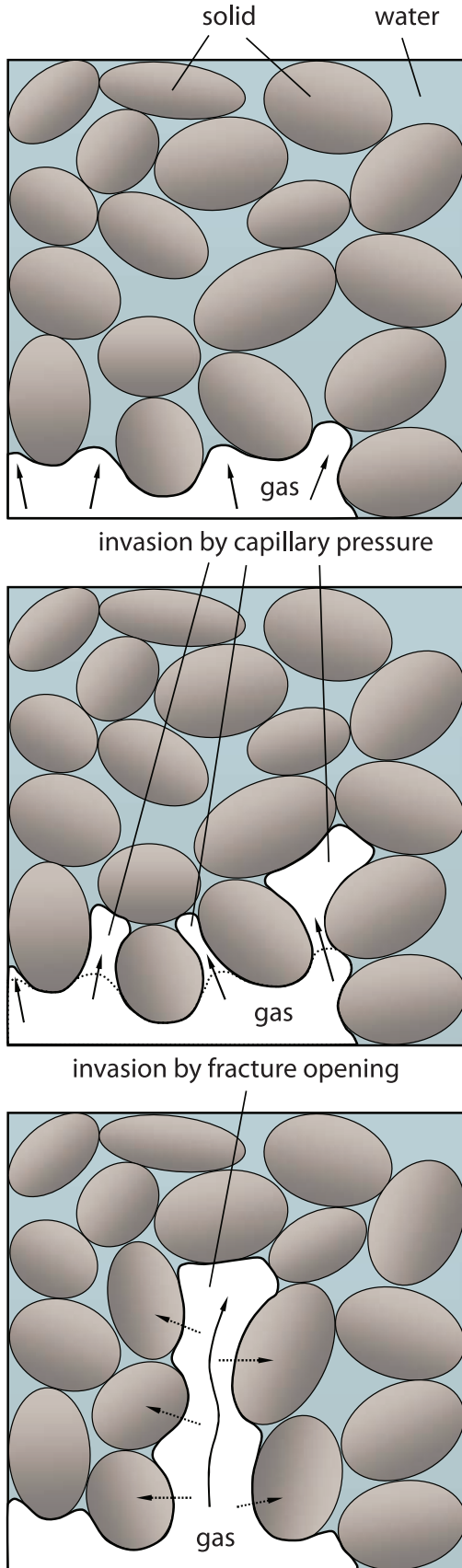
Figure 5. Schematic diagram of the two modes of methane gas invading a sediment. (top) Before invasion, the gas-water interface of a buoyant gas plume underlies water-filled sediment. (middle) Invasion will occur if the capillary pressure (the difference between gas pressure and water pressure) exceeds the capillary entry pressure, which is inversely proportional to the pore diameter. (bottom) Invasion by fracture opening; if the exerted pressure is sufficient to overcome compression and friction at grain contacts, a fracture will form. In a multiphase environment, due to surface tension effects, the pressure difference between water and gas will not dissipate quickly through the porous medium, and water at grain contacts will increase cohesion.

additional cohesion due to surface tension
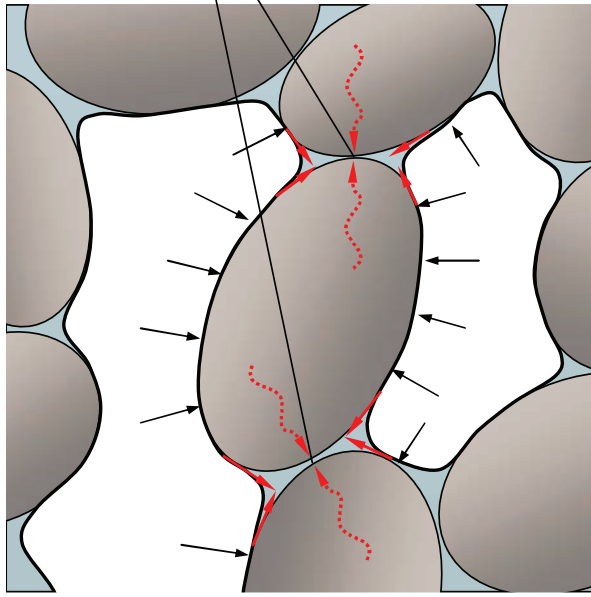
Figure 6. Meniscus pinning in the presence of two fluid phases in the sediment. During multiphase flow in porous media, the least wetting phase (gas, white) migrates through the center of the pores, while the most wetting phase (brine, blue) coats the grains (gray) and forms filaments around the crevices of the pore space. This configuration leads to gas-water menisci around the grain contacts. Because of interfacial tension (solid red arrows), these menisci are responsible for an attraction force between grains (dotted red arrows). At the macroscopic level, this can be interpreted as an increment in the cohesion of the material. This is a purely multiphase flow effect, not present in single-phase poromechanics.

typically not a favored scenario in single-fluid systems (unless a fluid is injected at very fast flow rates and pressures, as in hydraulic fracturing operations), it is natural in two-fluid systems because the two fluids have different pressures. Before a water-saturated pore is invaded by gas, the pore pressure forces correspond to the water pressure. Once the pore is invaded by gas, it is the gas pressure that exerts a net force onto the surrounding grains. Since the two fluids do not mix, a pressure difference does not dissipate. This pressure difference may lead to preferential fracturing of the sediment. These processes clearly couple flow and deformation, at both the grain scale and the macroscopic scale.

2.3.1. Capillary Invasion

[27] Consider invasion of methane free gas by capillary invasion (Figure 5 (middle)). The gas/water interface will invade a throat if the capillary pressure (that is, the difference between gas pressure and water pressure) is larger than the capillary entry pressure [*Richards*, 1931; *Leverett*, 1941; *Mayer and Stowe*, 1965]. The capillary entry pressure is proportional to the interfacial tension γ, and inversely proportional to the throat opening. Let d be the throat gap (which, in a 2-D model, may be negative if there is overlap between the grains). In Appendix B, we

derive the following expression for the gas pressure to invade a throat:

$$p_g - p_w \geq \frac{2}{\sqrt{1 + \left(1 + \frac{d}{2r_g}\right)^2} - 1} \frac{\gamma}{r_g}. \tag{15}$$

2.3.2. Fracture Opening

[28] Clearly, if the grain size is large, the process of capillary invasion is favored and gas invasion can occur even if the porous medium is rigid. In this case, the gas invasion pressure into the sediment is given by equation (15). On the other hand, for small grain size (high capillary entry pressures), gas invasion will not occur until the grains are pushed apart (Figure 5, bottom).

[29] For an idealized scenario of cohesionless material under undrained plane-strain conditions, a fracture will propagate when the gas pressure exceeds the minimum compressive stress (assumed horizontal):

$$p_g - \sigma_H \geq 0. \tag{16}$$

This fracture opening condition must be extended to the case when cohesion $\overline{\sigma}_c$ exists. In porous media filled with a single fluid, the source of cohesion (tensile strength) is grain cementation and consolidation. When the pore space is occupied by two fluids of different wettability, capillary forces induce additional adhesion between particles (Figure 6) [*Orr et al.*, 1975; *Lian et al.*, 1993; *Cho and Santamarina*, 2001].

[30] Because there is stress concentration at the fracture tip, the fracturing pressure depends not only on the earth stresses and the cohesive stress, but also the fracture's length. In the realm of linear elastic fracture mechanics (LEFM), the fracturing pressure is

$$p_g - \sigma_H \geq C_{\text{LEFM}} \frac{K_{Ic}}{\sqrt{\pi a}}, \tag{17}$$

where K_{Ic} is the fracture toughness, a is the length of the fracture, and C_{LEFM} is a coefficient that depends on the geometry, the ratio of horizontal to vertical stresses, and loading conditions [*Anderson*, 1991]. In the context of particle assemblies, the "measurable" fracture toughness depends on the cohesive strength (and, therefore, on the interfacial tension between fluids) and on the grain size. This last dependency emanates from the observation that the internal length scale in the fracture toughness is determined by the grain size [*Potyondy and Cundall*, 2004]. Therefore, under the assumptions of LEFM, the gas pressure for fracture opening takes the form

$$p_g - \sigma_H \geq C_{\text{LEFM}} \frac{\gamma \sqrt{r_g}}{r_g \sqrt{\pi a}}. \tag{18}$$

Even though LEFM conditions do not always apply to natural sediments, equation (18) indicates that asymptotically, $p_g^{\text{frac}} - \sigma_H \sim r_g^{-1/2}$. Equation (15) says that the gas pressure for capillary invasion scales like $p_g^{\text{cap}} - p_w \sim r_g^{-1}$. Both invasion pressures increase as the grain size decreases, but the capillary invasion pressure increases faster. This
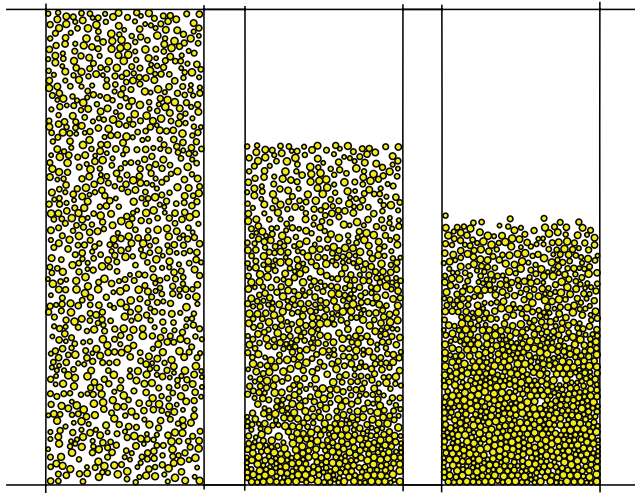
Figure 7. Snapshots of the particle settling process.

analysis suggests that fracturing is favored over capillary invasion for fine-grained sediments.

[31] In any case, we do not use LEFM. It is the nonlinear evolution of the DEM microporomechanical model that determines when bonds break, and when the gap between grains is large enough for the gas interface to advance, according to equation (15). In this fashion, the gas/water interface advances and a new pore is loaded with a higher pressure. The implementation of multifluid poromechanics is therefore very similar to that of single-fluid systems, except that the key hydraulic property (the conductance between pore bodies) is set to zero until condition (15) is satisfied.

[32] Capillary invasion and fracture opening are the two end-member mechanisms for methane transport in its own gas phase, and our coupled grain-scale model allows us to investigate the competition between the two as a function of grain size, earth stresses, and sediment cohesion.

3. Results

3.1. Micromechanics of "Dry" Media

3.1.1. Sediment Model Generation and Initialization

[33] A model sediment is generated by first choosing the number of particles, and reproducing the desired grain size distribution. As we show in section 3.1.2, several macroscopic properties (both mechanical and fluid flow properties) are dependent on the grain size. Therefore, it is important that the sediment model either reproduces the desired grain size distribution, or that the assigned microproperties (e.g., bond strength) reflect the disparity in grain size [*Potyondy and Cundall*, 2004]. In most of the examples shown in this paper, we have chosen a relatively narrow, uniform grain radius distribution [r_{min}, r_{max}], with $r_{max} = (5/3)r_{min}$.

[34] The particles are randomly placed in a box and allowed to fall under gravity, simulating sedimentation (Figure 7). The settling process has two differentiating stages: (1) free fall under gravity, with limited grain-grain interaction, and (2) settling and grain rearrangement until static conditions are reached.

[35] The time step is larger initially, during the "free fall" stage, and quickly converges to the value required for stability of the dynamical system dominated by grain-grain interactions. The time step is proportional to the grain radius, and inversely proportional to the square root of the grain stiffness, confirming the stability condition of equation (7).

3.1.2. Uniaxial Compaction for "Dry" Media

[36] Here we show that DEM simulations of "dry" media (infinitely compressible pore fluid) are able to capture the mechanical behavior of real sediments. In Figure 8 we plot experimental stress-strain curves of sediment samples from Hydrate Ridge [*Tan et al.*, 2006] along with curves from DEM simulations. The data come from triaxial tests that reproduce constant rate of strain (CRS) conditions, in which the lateral stress was also measured. The DEM model was created by sedimenting particles, and applying an isotropic confining stress of 20 kPa, to start the uniaxial vertical compaction test at the same stress level as the experiments [*Tan*, 2004]. The only parameter that we varied to reproduce measured stress-strain behavior was the grain stiffness k_n. The rest of the micromechanical parameters are as follows: $k_s = k_n$, $\overline{\mu} = 0.5$, $\overline{\sigma}_c = \overline{\tau}_c = 0$.

[37] The DEM simulations match the stress-strain behavior measured in the lab even for very high deformations (up to 16% strain), capturing the material nonlinearity. For an undisturbed ideal clay sample, the initial portion of the strain-log stress curve would be a straight line with slope equal to the unload/reload loop slope until reaching its preconsolidation stress. After this point, the slope would change to the virgin consolidation line slope. The Hydrate Ridge samples exhibit a large "rollover" at small strains (in the plot of vertical strain versus effective vertical stress on a logarithmic scale) because they are highly disturbed [*Tan*, 2004]. For the purpose of validation of the DEM model, the
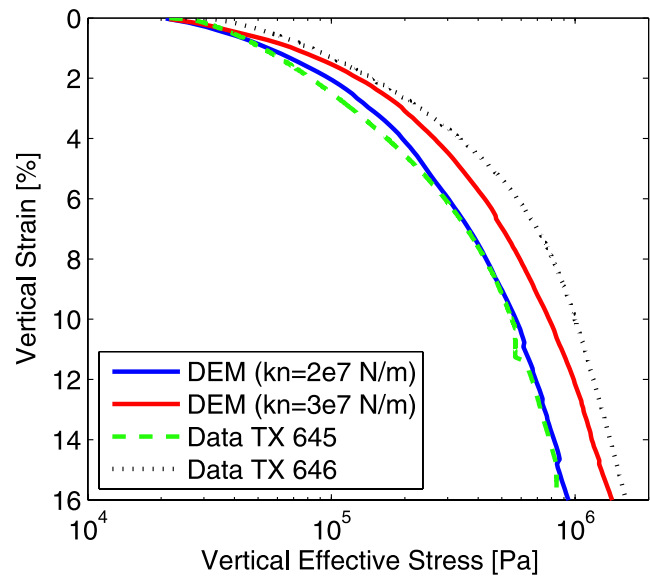
Figure 8. Experimental stress-strain curves for sediments from Hydrate Ridge [*Tan et al.*, 2006] and comparison with DEM simulations for two different values of the grain stiffness.
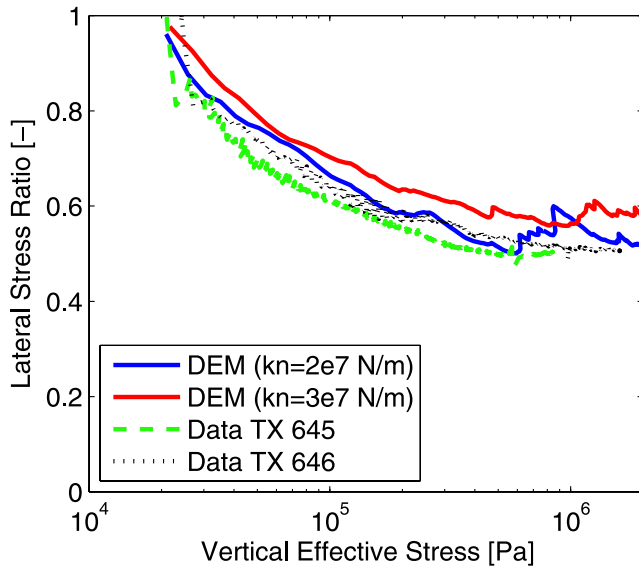
Figure 9. Experimental lateral-to-vertical stress ratio curves for sediments from Hydrate Ridge [*Tan et al.*, 2006] and comparison with DEM simulations for the same values of grain stiffness used to match the vertical stress-strain behavior in Figure 8.

relevant portion of the curve is that above the preconsolidation stress.

[38] Although we do not show it here, the DEM model also displays irreversible behavior in that loading/unloading cycles show hysteresis. However, it is unable to reflect the dramatic increase in stiffness upon unloading that the data show [*Jain and Juanes*, 2008].

[39] We also compared the lateral-to-vertical stress ratio, K_0, predicted by the DEM model with the values measured for Hydrate Ridge sediment samples [*Tan et al.*, 2006]. The stress ratio is measured during 1-D consolidation in triaxial cells. In preparation for the test, and to make sure the sample is fully saturated, initial vertical and horizontal effective stresses were brought to about 20 kPa (which is small enough that there is not significant strain) to remove any bubbles from the sample. To reproduce these conditions, we isotropically consolidated the DEM samples to 20 kPa as well prior to performing the 1-D consolidation. Therefore, the initial K_0 value is 1. We used the same grain stiffness parameters employed to match the lab stress-strain behavior (Figure 8), and we let the DEM model predict the evolution of the K_0 ratio for those experimental conditions (Figure 9). While the agreement between model and experiments is generally good, the experimentally measured values drop down to about 0.5, while those predicted by the DEM model drop to about 0.6.

3.2. Microporomechanics of Single-Fluid Systems
3.2.1. Uniaxial Fluid Flow

[40] In this section, we evaluate the fluid flow capabilities of the grain-scale model. We do so by simulating a one-dimensional fluid flow problem in a cell with drained top and bottom boundaries, and impervious fixed lateral boundaries. The initial pressure is constant, and equal to the boundary pressures. Suddenly, a pressure change is applied

to the top boundary, and we simulate the evolution of the pressure and fluid inflow/outflow until a new steady state is reached. The continuum problem is described mathematically by the partial differential equation:

$$c_v \frac{\partial p}{\partial t} - \frac{k}{\mu} \frac{\partial^2 p}{\partial x^2} = 0, \quad 0 < x < H, \tag{19}$$

where x is elevation, H is the height of the cell, k is the intrinsic permeability, μ is the fluid viscosity, and c_v is the consolidation coefficient [*Wang*, 2000]. The initial condition is given by

$$p(x, 0) = 0, \quad 0 \le x \le H, \tag{20}$$

and the boundary conditions are

$$p(0, t) = 0, \quad p(H, t) = \Delta p, \quad t > 0. \tag{21}$$

The problem can be expressed in dimensionless form by defining the following dimensionless quantities:

$$\begin{aligned}
\text{Distance} \quad & \xi = \frac{x}{H}, \\
\text{Time} \quad & \tau = \frac{t}{T_c}, \quad T_c = \frac{c_v \mu H^2}{k}, \\
\text{Pressure} \quad & p_D = \frac{p}{\Delta p}, \\
\text{Flow rate} \quad & Q_D = \frac{Q}{Q_c}, \quad Q_c = \frac{k}{\mu} \frac{\Delta p}{H} W w,
\end{aligned}$$

where W is the width and w is the thickness of the cell (that is, the dimensions of the cell in the directions perpendicular to the flow). The analytical solution to the problem can be found by the method of separation of variables [*Crank*, 1975]. The dimensionless pressure field is given by

$$p_D(\xi, \tau) = \xi + \frac{2}{\pi} \sum_{n=1}^{\infty} \frac{(-1)^n}{n} \sin(n\pi\xi) \exp\left(-(n\pi)^2 \tau\right). \tag{22}$$

By differentiating the expression above, we find the expression for the dimensionless flow rate in and out of the cell:

$$Q_D^{\text{in}} = 1 + 2 \sum_{n=1}^{\infty} (-1)^n \cos(n\pi) \exp\left(-(n\pi)^2 \tau\right), \tag{23}$$

$$Q_D^{\text{out}} = 1 + 2 \sum_{n=1}^{\infty} (-1)^n \exp\left(-(n\pi)^2 \tau\right). \tag{24}$$

[41] The objective is to determine whether the grain-scale model reproduces the macroscopic behavior. The relevant macroscopic parameters are the intrinsic permeability k and the consolidation coefficient c_v. The intrinsic permeability is obtained by matching the flow rate at steady state. The consolidation coefficient is determined by matching the dimensionless inflow and outflow curves.

[42] We generated an assembly with 1000 grains, and a minimum radius $r_{\text{min}} = 1$ cm. The vertical and horizontal
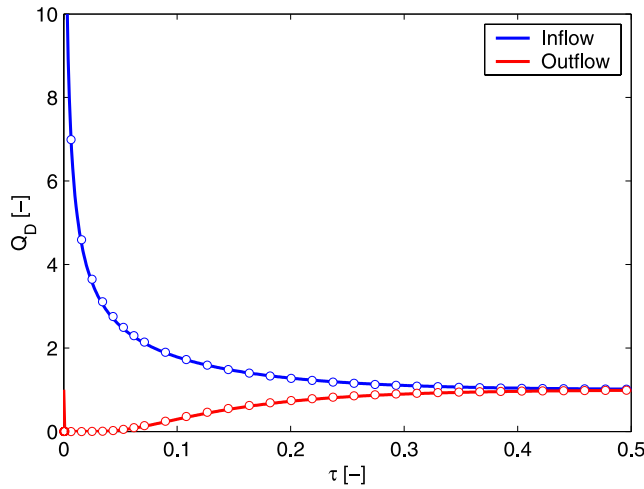
Figure 10. Inflow and outflow rates into the pressure cell. Comparison of DEM simulation (circles) and analytical solution (solid line).

dimensions of the cell are, approximately, $H = 1$ m and $W = 0.7$ m. We set the pressure increment Δp to a small value, so that the effects of pore pressure on the mechanical deformation are minimal. Once the flow stabilizes, inflow and outflow rates are equal to Q_c, and the intrinsic permeability of the medium can be computed as

$$k = \frac{\mu H Q_c}{W w \Delta p}. \qquad (25)$$

The characteristic time T_c is then obtained by matching the numerical inflow and outflow curves, from which the macroscopic consolidation coefficient is computed as

$$c_v = \frac{k T_c}{\mu H^2}. \qquad (26)$$

[43] In Figure 10 we plot the dimensionless inflow and outflow rates as a function of dimensionless time. The agreement between the DEM results and the analytical solution is excellent, indicating the flow formulation accurately captures the macroscopic behavior (Darcy flow in porous media). As a further validation of the model, we compare in Figure 11 the evolution of dimensionless pore pressure within the sample. By plotting the pressure values from the DEM simulation at individual pores, we obtain a scattered profile of the average pressure as a function of depth. We compare these results with the analytical solution at different dimensionless times. Again, the agreement is excellent.

[44] By repeating the fluid flow simulations with different values of r_{min}, we determine the dependence of the hydraulic and poromechanical parameters on grain size. The results are compiled in Table 1, where we confirm that the intrinsic permeability scales with the square of the grain size (as expected from Stokes theory, and the Kozeny-Carman relation for granular materials). Moreover, if the fluid is significantly more compressible that the skeleton, the DEM simulations also reflect that the effective consolidation coefficient c_v is inversely proportional to K_f, with the
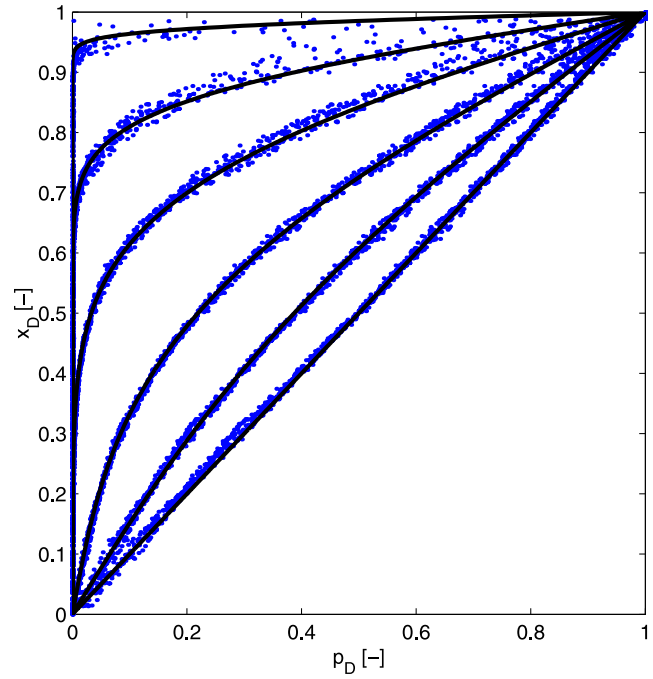
Figure 11. Evolution of pressure profiles during the uniaxial fluid flow test. Comparison of DEM simulation (dots) and analytical solution (solid line) at different dimensionless times: $\tau = 0.000242$ (top curve), 0.00671, 0.0275, 0.0829, 0.175, 1.404 (bottom curve).

constant of proportionality being approximately equal to the porosity [*Wang*, 2000].
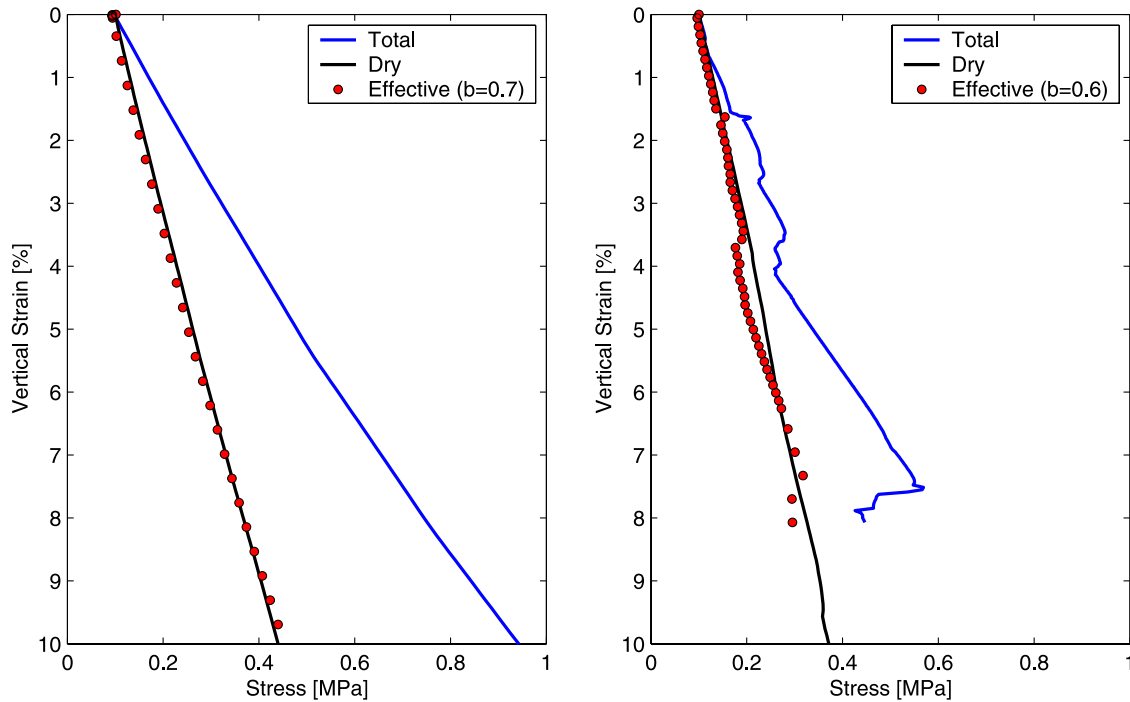
3.2.2. Uniaxial Undrained Compaction

[45] A sensitive test of the DEM coupled model's validity is fluid-solid behavior during undrained consolidation tests. A sediment model is initialized by gravitational settling. Then the walls are adjusted to achieve an isotropic confining stress state of 0.1 MPa (above atmospheric pressure). Until that point, the fluid is allowed to drain and the pore pressure is atmospheric ($p = 0$). Thus, the initial effective stress is 0.1 MPa. After that, the sample is sealed so that no fluid is allowed to drain, and it is subjected to uniaxial compaction. During the undrained compaction process, the vertical strain ε, total vertical stress σ, and average pore pressure p are recorded. In view of the effective stress concept [*Terzaghi*, 1943; *Biot*, 1941], the total stress required to achieve a given deformation in a fluid-saturated medium is larger than for a dry medium. In the realm of the linear theory of poroelasticity, the effective stress is given by

$$\sigma' = \sigma - bp, \qquad (27)$$

where b is the Biot coefficient. The dependence of the Biot coefficient on the solid and fluid properties of the

Table 1. Macroscopic Hydraulic and Poromechanical Parameters for Different Grain Size Distributions

r_{min} (m)	k (m^2)	c_v / K_f
0.01	0.289×10^{-6}	0.161
0.001	0.289×10^{-8}	0.156

Figure 12. Stress-strain curves for uniaxial undrained compaction. The total stress in the fluid-filled sample (blue solid line) is higher than the stress in the "dry" sample (black solid line). The effective stress curve (red circles) is obtained by subtracting the pore pressure (not plotted) premultiplied by the Biot coefficient from the total stress. An appropriate value of the Biot coefficient is found by matching the effective stress curve with the "dry" stress curve. (left) Cemented/cohesive sample. (right) Unconsolidated/cohesionless sample.

constituents is reasonably well understood [*Coussy*, 1995; *Wang*, 2000]. The Biot coefficient approaches a value of one only in the limit of incompressible grains and point grain-grain contacts. If the grain and fluid compressibilities are comparable, the Biot coefficient is less than one.

[46] We used an assembly with 1000 grains, $r_{min} = 0.01$ m, $k_n = 10^7$ N/m, $k_n/k_s = 2.5$, and $K_f = 10^7$ Pa. In Figure 12 we show the stress-strain curves for a cemented/cohesive sample (bond strength $\overline{\sigma}_c = \overline{\tau}_c = 10^6$ Pa, Figure 12, left), and for an unconsolidated/cohesionless sample (bond strength $\overline{\sigma}_c = \overline{\tau}_c = 10^2$ Pa, Figure 12, right). In both cases, we plot the stress-strain curves for the fluid-saturated medium (total stress), and for a dry medium. We confirm that the dry stress curve can be interpreted as the effective stress, and recovered by subtracting the pore pressure times the Biot coefficient from the total stress. We infer the Biot coefficient in this way, and the values obtained agree well with experimental values [*Wang*, 2000, Table C.1].

3.3. Microporomechanics of Two-Fluid Systems

[47] Migration of a gas phase through a deformable medium may occur by two end-member mechanisms: (1) capillary invasion through a rigid medium and (2) fracture opening. Our DEM model is capable of reproducing both mechanisms, and can therefore predict the conditions under which one is favored over the other, and predict gas migration as a result of their combined effect.

3.3.1. Capturing the Fracturing Phenomenon

[48] We first illustrate that our DEM model of coupled two-phase fluid flow and grain mechanics can reproduce fracture initiation and propagation upon invasion of an immiscible gas phase.

[49] In many (passive) depositional environments, the horizontal stress is lower than the vertical stress. In such scenarios, one expects the development of vertical fractures that open up the sediment in the direction of minimum compressive stress. In Figure 13 we show that fracturing of the sediment is not necessarily restricted to anisotropic earth stresses. Even when horizontal and vertical stresses are equal, the medium tends to fracture in a set of radial, geometrically complex fractures if gas is injected into a brine-saturated sediment.

3.3.2. Fracturing Versus Capillary Invasion: Influence of Grain Size

[50] We find the most sensitive factor in determining the mode of methane gas transport (sediment fracturing or capillary invasion) is the grain size: fracturing is favored for fine-grained sediments, while capillary invasion is favored for coarse-grained sediments. Here we illustrate these two end-members.

[51] The simulation is set up as follows. A sample of 300 grains of grain size $[r_{min}, 2r_{min}]$ is generated by gravitational settling. Since the sample size is much smaller than a representative elementary volume of sediment, we only simulate a narrow range of grain sizes at a time. The lateral boundaries are fixed. The sediment is then compacted vertically under constant pore pressure until a vertical effective stress of 3 MPa is achieved. This level of vertical effective stress corresponds to a depth of about 300 m below seafloor. During this vertical compaction, the
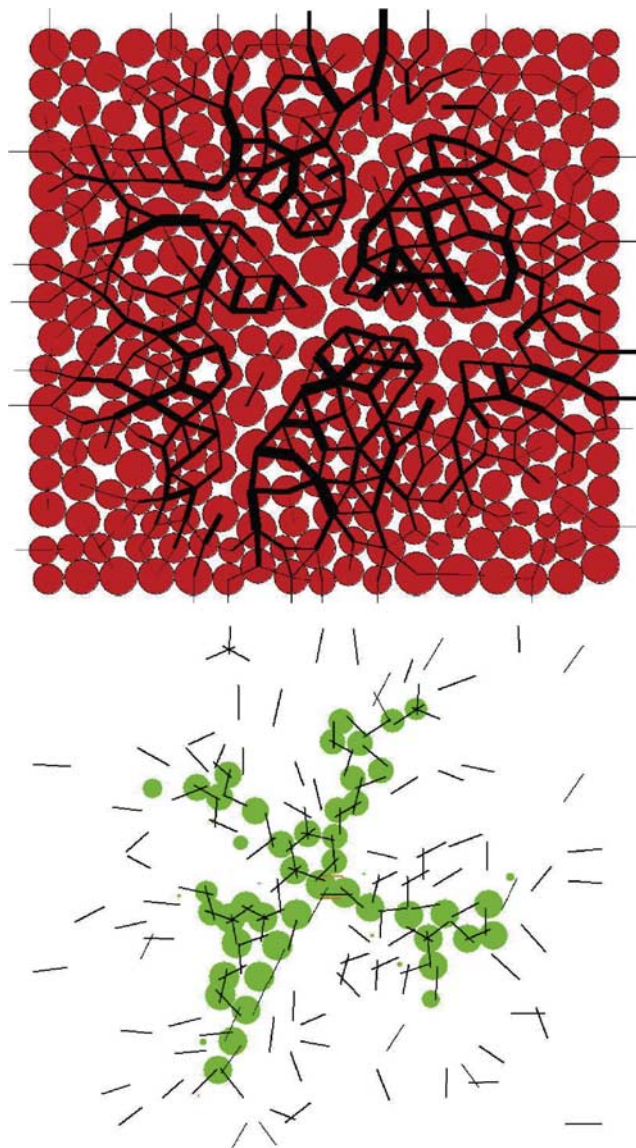
Figure 13. Illustration of the fracturing behavior of a model sediment upon injection of gas when the vertical and horizontal stresses are equal. The sediment fractures "isotropically" into a set of radial, geometrically complex fractures. (top) The grain assembly (red circles) after fracturing due to "injection" of gas at the center of the domain. The thick black lines denote compressive forces at the grain-grain contacts. Note that they are missing from the fractured areas. (bottom) Representation of the pores occupied by the injected gas (green circles). The thin black lines indicate grain-grain contacts that have exceeded the contact strength and have therefore "broken." Note the complementary nature of this set of lines to that of the force network above.

horizontal effective stress increases to a value of about 1.6 MPa, that is, $K_0 \approx 0.53$. Inasmuch as gravitational effects are negligible in a grain-scale model, the results are independent of water depth; they depend on the relative magnitudes of capillary pressure (the difference between gas pressure and water pressure) and effective stress (the difference between the total stress and the pore pressure).

[52] The interfacial tension is $\gamma = 50 \times 10^{-3}$ N/m. We assume the cohesion is inversely proportional to grain radius. This is phenomenologically adequate (fine-grained material like clays are cohesive) and is also consistent with the adhesive forces that result from the presence of a gas-water interface [*Kato et al.*, 2004]. For simplicity, we take $\overline{\sigma}_c = 2\gamma/r_g$. The only parameter that is left free is the grain size r_{min}.

[53] During the simulation, we inject gas at the bottom center pore. We incrementally increase the gas pressure. Between each increment, we allow sufficient time to pass for fluid flow and granular displacements to stabilize, so mechanical equilibrium is reached.

[54] In Figure 14 we show two snapshots of the evolution of the methane-water interface for a coarse-grain sediment of characteristic size $r_{min} = 50$ μm. It is apparent that during the invasion of methane gas, there is virtually no movement of the solid grains: the sediment acts like a rigid skeleton. Indeed, the network of grain contact compressive forces remains the same during the process. Invasion of gas from pore to pore occurs when the gas pressure (minus the water pressure) exceeds the capillary entry pressure of the throat (equation (15)). In this case, the capillary entry pressure is much lower than the fracturing pressure (Figure 14 (left) corresponds to $P_c \approx 5$ kPa), and fluid transport is well described by invasion percolation [*Wilkinson and Willemsen*, 1983; *Lenormand et al.*, 1988]. Ultimately, if the gas pressure is sufficiently high, almost all the pores have been invaded by methane gas. In this case, this occurs at a slightly higher capillary entry pressure of $P_c \approx 6$ kPa.

[55] The behavior is completely different when a much smaller grain size is used. The evolution of the methane gas migration for $r_{min} = 0.1$ μm is shown in Figure 15. The range of capillary entry pressures for the initial configuration is now on the order of 3 MPa. However, at this pressure, mechanical effects become dominant, and the solid skeleton no longer behaves like a rigid medium. At $P_c \approx 2.5$ MPa, the invading gas starts to initiate a fracture, with its characteristic stress concentration at the fracture tip captured by the DEM model [*Potyondy and Cundall*, 2004]. The fracture propagates vertically. Animations S1 and S2 are movies of the developing fracture and are available in the auxiliary material.[1] The value of the capillary pressure needed to open the fracture corresponds to a gas column thickness of about 300 m below the base of the HSZ. Gas column thicknesses of this magnitude have been observed in similar geologic environments [*Holbrook et al.*, 1996; *Hornbach et al.*, 2004], and interpreted as the cause of critical pressures for gas migration through faults [*Flemings et al.*, 2003; *Hornbach et al.*, 2004; *Trehu et al.*, 2004a].

[56] Our grain-scale model explains why focused gas flow can occur by means of fracture opening, even in the absence of preexisting faults and fractures. It is likely, however, that our model overestimates the invasion capillary pressure required for fracturing, due to boundary effects. This can be seen from the grain forces on the lateral boundaries in Figure 15, which change significantly as the fracture propagates. This is confirmed by the increase of the vertical and, especially, horizontal mean effective stress

---

[1]Auxiliary materials are available in the HTML. doi:10.1029/2008JB006002.
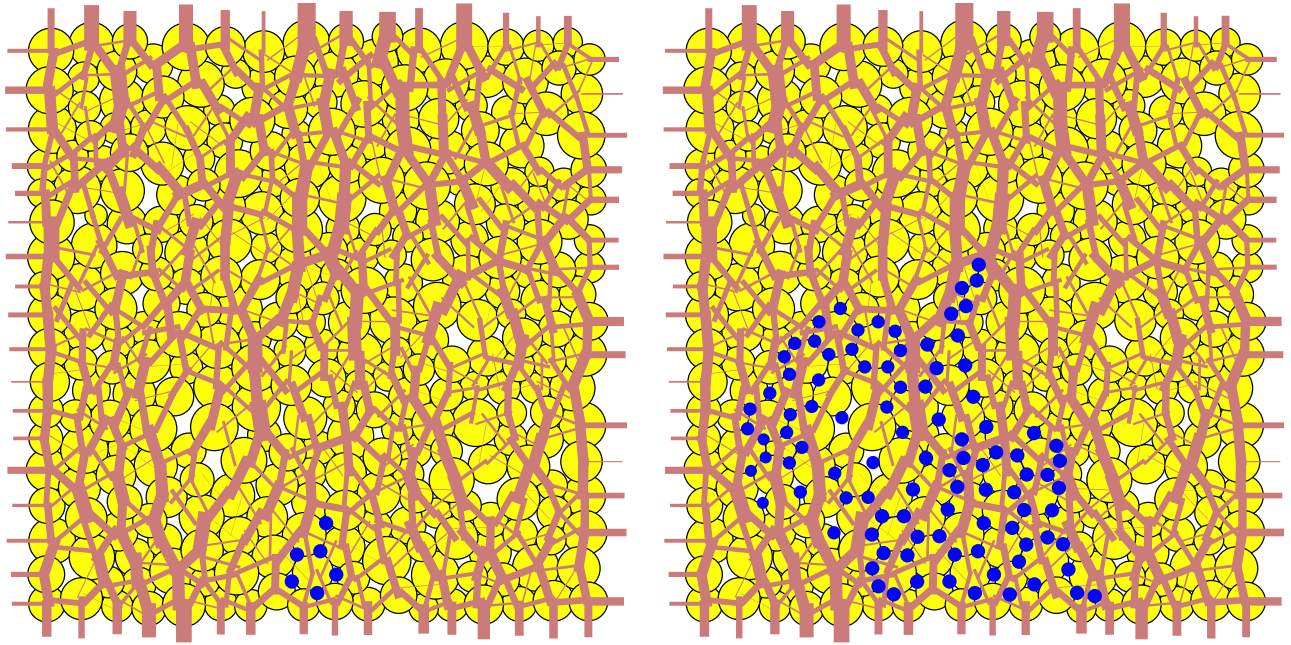
Figure 14. Snapshots of the evolution of the methane gas-water interface for the case $r_{min} = 50$ μm. The dominant mechanism is capillary invasion. The pores occupied fully by gas are represented with blue dots at the pore centers. The maroon lines indicate compression at grain-grain contacts. The green lines represent tension, which is supported by cohesion between grains. (left) $P_c = 5$ kPa. (right) $P_c = 6$ kPa.
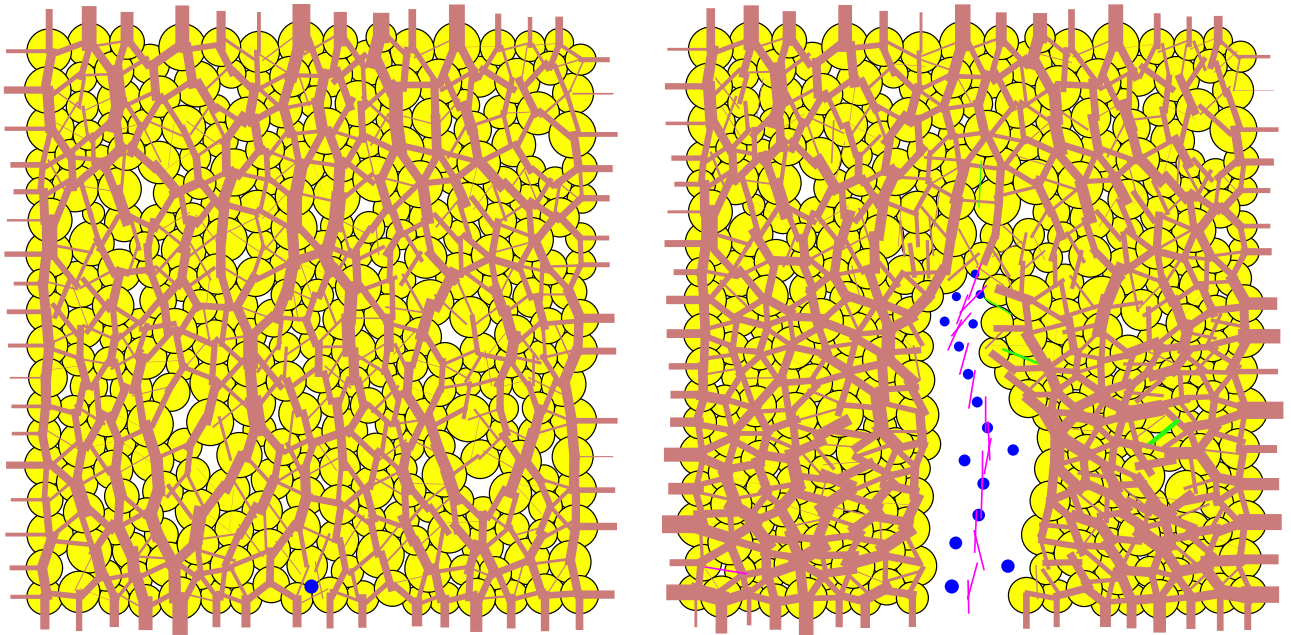
Figure 15. Snapshots of the evolution of the methane gas-water interface for an assembly with $r_{min} = 0.1$ μm. The dominant mechanism is fracture opening. The pores occupied fully by gas are represented with blue dots at the pore centers. The maroon lines indicate compression at grain-grain contacts. The green lines represent tension, which is supported by cohesion between grains. The pink lines show where cohesive bonds were broken. (left) $P_c = 2.5$ MPa. (right) $P_c = 2.55$ MPa. Movies of the developing fracture are available in the auxiliary material as Animation S2.
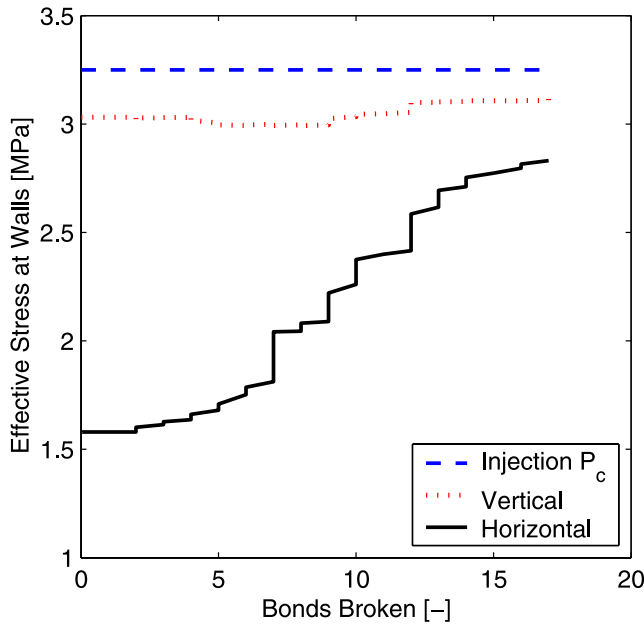
Figure 16. Evolution of the vertical and horizontal mean effective stress during fracture propagation for the simulation shown in Figure 15. The invading gas pressure remains constant throughout, but the vertical and, especially, the horizontal stress at the boundaries increase during fracture growth. The boundaries introduce an artificial stiffness in the problem that results in an overestimation of the gas invasion pressure.

during fracture growth (Figure 16). The presence of computational boundaries near the propagating fracture introduces an artificial stiffness to the problem.

4. Discussion and Conclusions

[57] We have presented a discrete element model for simulating, at the grain scale, gas migration in brine-saturated deformable media. The model has been validated for many processes, including (1) generating sediment models by gravitational settling and compaction; (2) stress-strain behavior of ocean sediments; (3) transient single-phase flow for determining hydraulic parameters; and (4) undrained compaction tests for determining poromechanical parameters.

[58] The coupled model permits investigating an essential process that takes place at the base of the hydrate stability zone: the upward migration of methane in its own free gas phase. We elucidate the two ways in which gas migration may take place: (1) by capillary invasion in a rigid-like medium and (2) by initiation and propagation of a fracture.

[59] Each end-member can be analyzed separately, and conditions for gas invasion can be found for the capillary-dominated and fracture-dominated regimes. We find the main factors controlling the mode of gas transport in the sediment are the grain size and the effective confining stress. We have shown that coarse-grain sediments favor capillary invasion, whereas fracturing dominates in fine-grain media. Recent laboratory experiments of gas invasion and bubble growth in soft, fine-grained sediments provide convincing evidence that fracturing is a relevant gas trans-

port mechanism [*Boudreau et al.*, 2005; *Best et al.*, 2006]. The cornflake-shaped, subvertical fractures observed in those experiments are strikingly similar to those simulated with the mechanistic grain-scale model presented here.

[60] The significant contribution of our coupled model is that it captures both phenomena and, as a result, allows us to study the transition between the two regimes. We synthesize the transition from capillary invasion to fracture opening in Figure 17. We plot the gas pressure required for invasion into a sediment at an effective confining stress of 3 MPa (typical of a sediment column depth of about 300 m) as a function of grain size. For sufficiently coarse grain size, gas invades by capillarity. According to equation (15), the invasion capillary pressure for this regime decreases with increasing grain size and has the following scaling:

$$P_c^{cap} \sim r_g^{-1}. \tag{28}$$
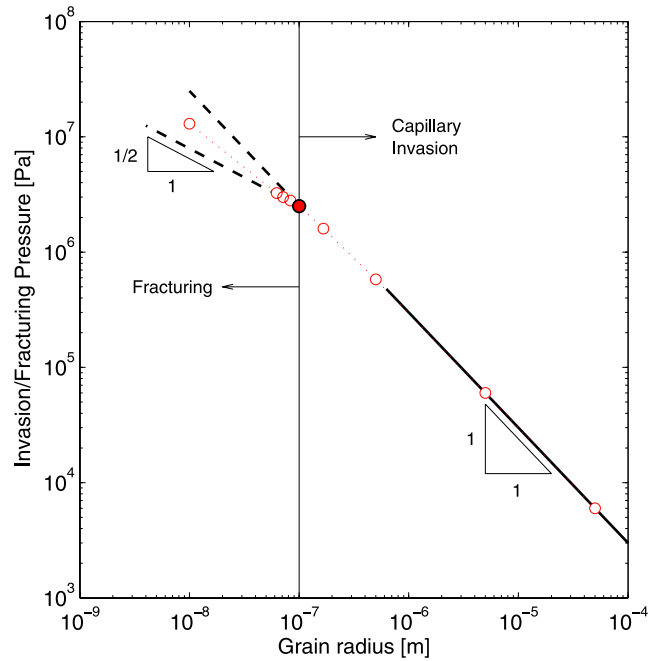
Figure 17. Plot of invasion pressure versus grain size (open red circles) for a sediment under 3 MPa vertical effective stress (sediment column depth of about 300 m). The solid red circle denotes the critical grain size at which the transition in the mode of gas invasion occurs. For larger grain size, gas invades by capillarity. For smaller grain size, it invades by opening a fracture. In the capillarity-dominated regime, the invasion capillary pressure decreases with increasing grain size with a slope of -1 (black solid line), consistent with the theory (equation (28)). In the fracture-dominated regime, the invasion capillary pressure increases with decreasing grain size, though the predictions of linear elastic fracture mechanics (black dashed line with slope $-1/2$) are not in agreement with our coupled grain-scale model. The deviation from linear-elastic fracture mechanics suggests that the effects of capillarity and inelastic material behavior are important but it may also be due to boundary effects in the grain-scale simulations.

This scaling is clearly confirmed by our DEM simulations, which collapse onto a straight line of slope -1 on the log-log plot of P_c versus r_g.

[61] There exists a critical grain size, in this case $r_g \approx 0.1 \ \mu$m, at which the transition from capillary invasion to fracturing occurs. For grain sizes below this critical value, invasion is always by fracture opening. The pressure required for opening a fracture, however, does depend on grain size. Under LEFM conditions, the expected scaling from equation (18) is

$$P_c^{\text{frac}} - \sigma_H' \sim r_g^{-1/2}, \qquad (29)$$

which corresponds to a straight line of slope $-1/2$. This behavior is not confirmed by our grain-scale model, which, unlike LEFM, accounts for the coupling between two-phase flow and inelastic grain-scale mechanics. This suggests that inelastic and capillary effects are essential in the fracturing process.

[62] These emergent phenomena have important implications for understanding hydrates in natural systems (either ocean sediments and permafrost regions). Our model predicts that in fine sediments, hydrate will likely form in veins that follow a fracture-network pattern. Since the mechanism of fracture propagation is self-reinforcing, our results indicate that it is possible, and even likely, that methane gas will penetrate deeply into the HSZ (and maybe all the way to the ground surface).

[63] Our model supports the view that in coarse sediments, the buoyant methane gas is likely to invade the pore space more uniformly, in a process akin to invasion percolation. While this is definitely affected by heterogeneity in grain size distribution, the overall pore occupancy is likely to be higher than for a fracture-dominated regime, leading to larger timescales for transport. The predictions from our model are consistent with field observations of hydrates in natural systems [*Suess et al.*, 1999; *Sassen et al.*, 2001; *Flemings et al.*, 2003; *Trehu et al.*, 2004a; *Hornbach et al.*, 2004; *Trehu et al.*, 2006a; *Riedel et al.*, 2006; *Weinberger and Brown*, 2006; *Liu and Flemings*, 2006, 2007; *Collett et al.*, 2008].

[64] We have not undertaken here an analysis on the relative importance of transport in solution versus as a separate free gas phase flowing through fractures. However, the importance of free gas fluxes through fractures is demonstrated by the massive free methane gas venting rates observed intermittently at northern Hydrate Ridge [*Torres et al.*, 2002]. *Tryon et al.* [1999, 2002] hypothesized that fracture networks rapidly transport the gas from beneath the HSZ to the vents, a distance of $70-100$ m. The total methane flux coming out of 10 discrete vents ($\sim$1 cm diameter each), clustered in a depression several meters in diameter, constitutes two thirds of the total flux, calculated from seawater methane concentrations in the overlying water column [*Heeschen et al.*, 2005]. Acoustic imaging shows massive bubble plumes at two other sites in the region [*Heeschen et al.*, 2005], which likely account for the remaining one third of the flux to the water column. Free gas ebullition through vents fed by fractures releases methane from the seafloor at rates many orders of magnitude faster than transport by advection of dissolved methane in

solution through sediments [*Torres et al.*, 2002]. In terms of velocities, the gas bubbles exit conduits episodically at about 1 m/s [*Torres et al.*, 2002], whereas pore water advection occurs at $0.5-1$ m/a, calculated from dissolved calcium profiles in sediment pore water, or $0.3-1$ m/a, calculated from seafloor methane seepage rates [*Torres et al.*, 2002], so free gas exits conduits more than 10^7 times faster than the speed of fluid advection in the sediments. At less active regions, like Blake Ridge, advective fluxes are 2 to 3 orders of magnitude slower than those at Hydrate Ridge [*Nimblett and Ruppel*, 2003].

[65] The results from this work also have important implications for carbon dioxide storage in the deep subseafloor, where sequestration is possible by hydrate formation [*Koide et al.*, 1995, 1997b] and gravitational trapping [*Koide et al.*, 1997a; *House et al.*, 2006; *Levine et al.*, 2007; *Goldberg et al.*, 2008]. Whether the migration of supercritical CO_2 is dominated by capillary invasion or fracture opening may determine the viability of this sequestration concept in ocean sediments. In these systems, fractures will have a tendency to propagate vertically [*Nunn and Meulbroek*, 2002; *Boudreau et al.*, 2005], which could provide fast pathways for the escape of injected CO_2 by pressure gradients. In order to avoid the fracturing regime, it is conceivable that one should inject in coarse-grained, high-energy sediments such as turbidites.

Appendix A: Throat Conductance

[66] In this section we derive equation (9) for the throat conductance. Our formulation resolves one fundamental problem of two-dimensional grain-scale models: the fact that when grains are in contact, the aperture of the throat between pores is zero. Three-dimensional models do not suffer from this problem, because the throat can be associated with the section of minimum cross-sectional area between two pore bodies.

[67] Before discussing our formulation for 2-D models, consider an individual pore throat in three dimensions, as shown in Figure A1. A throat can be considered a microfluidics pipe, with a certain angular cross section. For creeping flow in a small channel, the Navier-Stokes equations reduce to the elliptic Poisson equation. For a coordinate system in which one of the axes (say, the z axis) is parallel to the channel, the equation and boundary conditions describing the flow read [*Bird et al.*, 1960]

$$\nabla^2 v = -\frac{\Xi}{\mu} \quad \text{in} \quad \Omega, \qquad (A1)$$
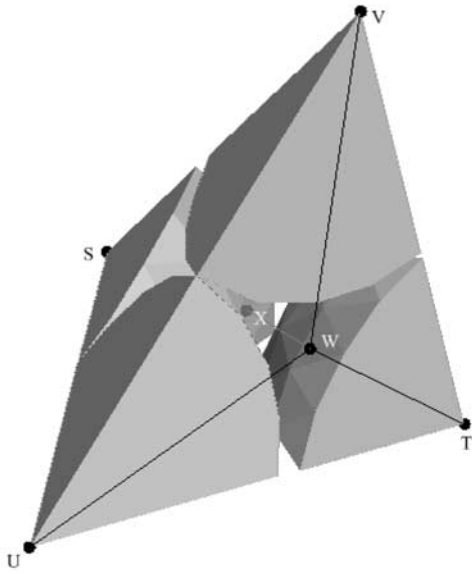
$$\Xi = -\frac{\partial p}{\partial z}, \qquad (A2)$$

$$v(x, y) = 0 \quad \text{on} \quad \partial\Omega, \qquad (A3)$$

where μ is the fluid viscosity, Ξ is the (negative) pressure gradient, and $\partial\Omega$ is the boundary of the two-dimensional cross section Ω.

[68] Many solutions to this equation exist for simplified geometries, and useful parameterizations have been devel-

Figure A1. Representation of a pore throat in a three-dimensional grain-scale model [*Prodanovic and Bryant*, 2006]. The throat is the section with minimum cross-sectional area between two pore bodies. This area is positive even when the surrounding grains are in contact, or even if they overlap.

oped in the context of pore network models of fluid flow through rocks [*Øren et al.*, 1998; *Patzek and Silin*, 2001]. The total flow rate q through the throat cross section can be expressed in the following form:

$$q \equiv \int_\Omega v(x,y)\, d\Omega = C\Xi, \qquad (A4)$$

where C is the throat conductance. Dimensional analysis dictates that the conductance can, in turn, be expressed as follows:

$$C = \frac{1}{\mu} A^2 \tilde{C}, \qquad (A5)$$

where A is the cross-sectional area of the throat, and $\tilde{C}$ is a dimensionless conductance. It has been shown that for a very wide range of throat shapes, the dimensionless conductance is simply a function of the shape factor,

$$G = \frac{A}{P^2}, \qquad (A6)$$

where P is the perimeter of the throat. In fact, for triangular cross sections, the dimensionless conductance can be approximated by the simple expression [*Patzek and Silin*, 2001]

$$\tilde{C} = \frac{3}{5} G. \qquad (A7)$$

[69] With precise knowledge of the geometry of the grain assembly, one could compute the area and shape factor for each throat, and evaluate the throat conductance using expressions (A5)–(A7). However, since these equations themselves rely on the assumption of creeping flow in cylindrical channels, it is sufficient to consider a "master" geometry (like the one shown in Figure A1). In any case, it is important to note that the throat conductance scales with the fourth power of the grain size:

$$C \sim \frac{\tilde{C}}{\mu} r_g^4. \qquad (A8)$$

[70] The question is How do we apply this conductance formulation to two-dimensional grain-scale models? In 2-D models, the cross section (or aperture) of a pore throat is zero if grains are in contact. This would lead to a model that does not conduct fluid. To address this issue, previous investigations typically resort to defining an artificial throat aperture using heuristic arguments [*Bruno and Nelson*, 1991; *Li and Holt*, 2001, 2004; *Itasca*, 2004].

[71] We resolve this problem by understanding a two-dimensional model as a collapsed three-dimensional model. We must make some approximations with respect to the grain arrangement in the third dimension. In particular, we assume cubic packing of the 3-D assembly. Consider two grains of the same size that are in contact in the 2-D model (Figure A2). For cubic packing in the third dimension, the geometry of the throats is well defined, and the flow rate through an individual throat can be computed with equations (A4)–(A5).

[72] Importantly, this model leads to physically realistic throat geometries (and, therefore, throat conductances) regardless of whether the two grains defining a throat are just in contact (gap $d = 0$), whether there is a gap between them ($d > 0$), or whether there is overlap between them ($d < 0$). For each configuration, the shape factor can be computed using elementary geometry, and the dimensionless conductance evaluated therefrom. In Figure A3, we summarize the throat conductance formulation for 2-D grain assemblies.

[73] In a 2-D model, we must collapse the third dimension, and compute the flow rate between pore bodies as

$$q_{2D} = q_{3D} \frac{w}{2r_g}, \qquad (A9)$$

where if $w = 1$, Q is the flow rate per unit width. Combining equation (A9) with (A4) and (A5) leads to equations (8) and (9), as desired.

Appendix B: Capillary Entry Pressure

[74] The conceptual model presented in Appendix A also provides a framework for determining capillary entry pressures in two-dimensional models, which is required to simulate two-phase flow.

[75] Consider, first, invasion of gas through a throat in a three-dimensional setting (Figure A1). The surface tension between gas and brine is γ, and the contact angle between the gas-water interface and the solid surface is θ. Gas will penetrate through the throat cross section when the capillary pressure (the gas pressure minus the water pressure) exceeds
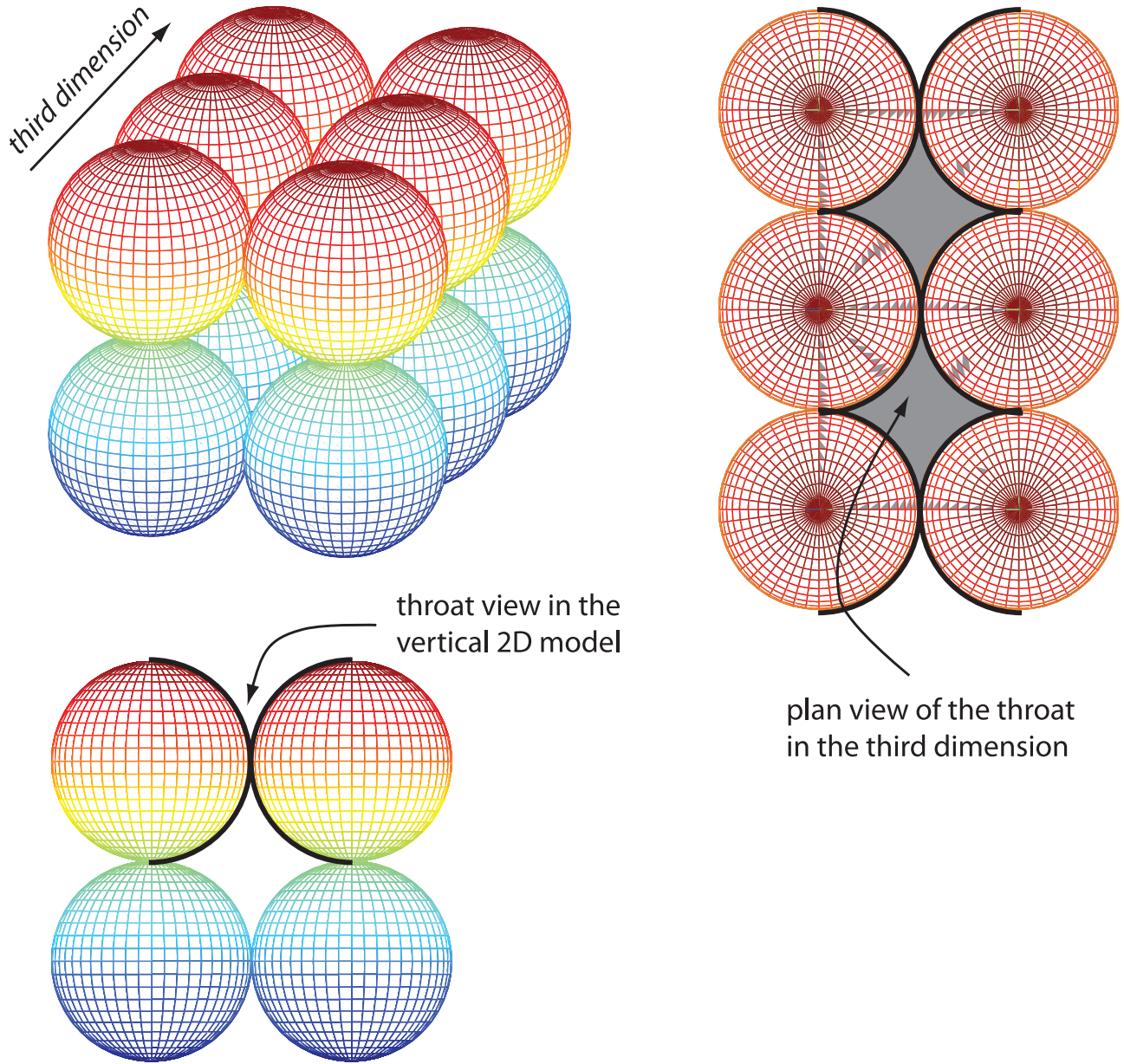
Figure A2. Schematic representation of our conductance model for two-dimensional assemblies, in which a physically based throat cross section is defined by assuming cubic packing in the third dimension. (bottom) Four grains of an idealized 2-D assembly. (top left) The model adopted in the third (collapsed) dimension. (top right) A top view of the conceptual 3-D model. It is apparent that this model leads to a well-defined pore throat (shaded in gray) even though the two grains are in contact in the vertical 2-D model.

the threshold capillary pressure. The Mayer-Stowe-Princen (MSP) [*Mayer and Stowe*, 1965; *Princen*, 1969a, 1969, 1970] method for calculating the threshold pressure relies on equating the curvature of the corner arc menisci to the curvature of the invading interface. Expressions for the drainage capillary entry pressure have been derived for a variety of cross sections [*Mason and Morrow*, 1991; *Øren et al.*, 1998; *Patzek*, 2001]. They take the form

$$P_c^e = \frac{2\gamma}{r_{\text{th}}} F(\theta, G, D), \tag{B1}$$

where r_{th} is the radius of the inscribed circle and F is a function of the receding contact angle and the geometry of the throat, through the throat shape factor G and a function D of the throat corner angles. It turns out that if the contact angle is small (as it normally is for gas invasion into a natural sediment), $F \approx 1$ [*Lenormand et al.*, 1983; *Patzek*, 2001]. Therefore, for zero contact angle, the capillary entry pressure can be approximated by

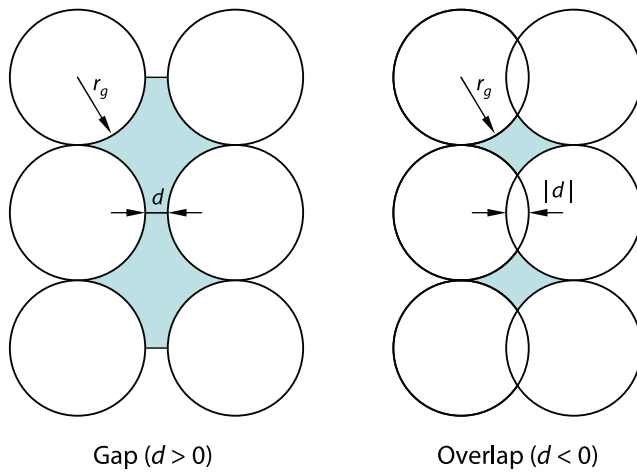$$P_c^e = \frac{2\gamma}{r_{\text{th}}}. \tag{B2}$$

For a throat formed in the space between three spherical grains of equal radius r_g that are in contact, elementary geometry leads to the expression

$$r_{\text{th}} = r_g\left(\frac{2}{\sqrt{3}} - 1\right), \tag{B3}$$

and, therefore, we obtain the simple and useful estimate:

$$P_c^e \approx 10\frac{\gamma}{r_g}. \tag{B4}$$

[76]　Once again, we apply this concept to two-dimensional grain-scale models, by assuming simple cubic packing in the third dimension. In this way, we can rigorously define a throat

Gap ($d > 0$)　　　　　Overlap ($d < 0$)

Figure B1. Geometry of the pore throat in the third dimension of a 2-D grain-scale model, for the definition of the throat radius r_{th}.

radius (and, from it, a capillary entry pressure) even when the 2-D throat aperture is zero (because the 2-D grains defining a pore throat are in contact). If the two grains are exactly in contact (see Figure B1), one can immediately obtain the relation

$$r_{\text{th}} = r_g\left(\sqrt{2} - 1\right). \tag{B5}$$

When the two grains of equal size are separated by a gap ($d > 0$), or when they overlap ($d < 0$), relation (B5) can be extended as follows:

$$r_{\text{th}} = r_g\left(\sqrt{1 + \left(1 + \frac{d}{2r_g}\right)^2} - 1\right). \tag{B6}$$

Substituting equation (B6) into (B2) leads to equation (15), as desired.

References

Anderson, A. L., and L. D. Hampton (1980), Acoustics of gas-bearing sediments. 1. Background, *J. Acoust. Soc. Am.*, *67*(6), 1865–1889, doi:10.1121/1.384453.

Anderson, A. L., F. Abegg, J. A. Hawkins, M. E. Duncan, and A. P. Lyons (1998), Bubble populations and acoustic interaction with the gassy floor of Eckernförde Bay, *Cont. Shelf Res.*, *18*, 1807–1838, doi:10.1016/S0278-4343(98)00059-4.

Anderson, T. L. (1991), *Fracture Mechanics: Fundamentals and Applications*, CRC Press, Boca Raton, Fla.

Archer, D., B. Buffett, and V. Brovkin (2009), Ocean methane hydrates as a slow tipping point in the global carbon cycle, *Proc. Natl. Acad. Sci. U.S.A.*, doi:10.1073/pnas.0800885105, in press.

Behseresht, J., Y. Peng, M. Prodanovic, S. L. Bryant, A. K. Jain, and R. Juanes (2008), Mechanisms by which methane gas and methane hydrate coexist in ocean sediments, paper OTC 19332 presented at Offshore Technology Conference, Offshore Technol. Conf., Houston, Tex.

Gap ($d > 0$)　　　　　Overlap ($d < 0$)

If $d > 0$ (gap)

$$A = 4r_g^2\left(1 - \frac{\pi}{4} + \frac{d}{r_g}\right)$$

$$P = 2r_g\left(\pi + \frac{2d}{r_g}\right)$$

Elseif $d \leq 0$ (overlap)

$$A = 4r_g^2\left(1 - \sqrt{\frac{|d|}{r_g} - \left(\frac{|d|}{2r_g}\right)^2}\right)\left(1 - \frac{|d|}{r_g}\right)$$

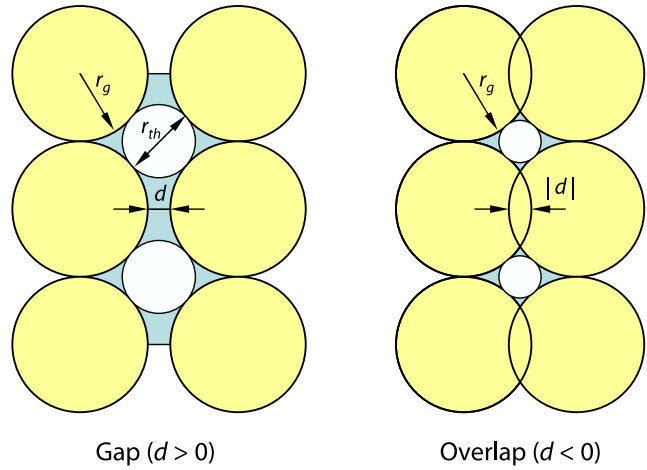$$\alpha = \sin^{-1}\left(1 - \frac{|d|}{2r_g}\right)$$

$$P = 2r_g \cdot 2\alpha$$

Endif

$$G = \frac{A}{P^2}$$

$$\tilde{C} = \frac{3}{5}G$$

Figure A3. Summary of the throat conductance formulation for 2-D grain assemblies. Top view of the cross-sectional area of the throat in the collapsed 3-D model. (See text for the definition of the variables and a discussion of the formulation.)

Best, A. I., M. D. Richardson, B. P. Boudreau, A. G. Judd, I. Leifer, A. P. Lyons, C. S. Martens, D. L. Orange, and S. J. Wheeler (2006), Shallow seabed methane gas could pose coastal hazard, *Eos Trans. AGU*, *87*(22), 213,217.

Biot, M. A. (1941), General theory of three-dimensional consolidation, *J. Appl. Phys.*, *12*, 155–164, doi:10.1063/1.1712886.

Bird, R. B., W. E. Stewart, and E. N. Lightfoot (1960), *Transport Phenomena*, John Wiley, New York.

Boudreau, B. P., C. Algar, B. D. Johnson, I. Croudace, A. Reed, Y. Furukawa, K. M. Dorgan, P. A. Jumars, and A. S. Grader (2005), Bubble growth and rise in soft sediments, *Geology*, *33*(6), 517–520, doi:10.1130/G21259.1.

Bruno, M. S. (1994), Micromechanics of stress-induced permeability anisotropy and damage in sedimentary rocks, *Mech. Mater.*, *18*, 31–48, doi:10.1016/0167-6636(94)90004-3.

Bruno, M. S., and R. B. Nelson (1991), Microstructural analysis of the inelastic behavior of sedimentary rock, *Mech. Mater.*, *12*(2), 95–118, doi:10.1016/0167-6636(91)90057-7.

Buffett, B., and D. Archer (2004), Global inventory of methane clathrate: sensitivity to changes in the deep ocean, *Earth Planet. Sci. Lett.*, *227*, 185–199, doi:10.1016/j.epsl.2004.09.005.

Cho, G. C., and J. C. Santamarina (2001), Unsaturated particulate materials—Particle-level studies, *J. Geotech. Geoenviron. Eng.*, *127*(1), 84–96.

Collett, T., et al. (Eds.) (2008), Indian National Gas Hydrate Program Expedition 01 Initial Reports, Indian Dir. General of Hydrocarbons, New Delhi, India.

Cook, B. K., D. R. Noble, and J. R. Williams (2004), A direct simulation method for particle-fluid systems, *Eng. Comput.*, *21*(2–4), 151–168.

Coussy, O. (1995), *Mechanics of Porous Media*, John Wiley, Chichester, U. K.

Crank, J. (1975), *Mathematics of Diffusion*, 2nd ed., Oxford Univ. Press, New York.

Cundall, P. A., and O. D. L. Strack (1979), Discrete numerical model for granular assemblies, *Geotechnique*, *29*, 47–65.

Dickens, G. R. (2003), Rethinking the global carbon cycle with a large, dynamic and microbially mediated gas hydrate capacitor, *Earth Planet. Sci. Lett.*, *213*, 169–183, doi:10.1016/S0012-821X(03)00325-X.

Dickens, G. R., J. R. O'Neil, D. K. Rea, and R. M. Owen (1995), Dissociation of oceanic methane hydrate as a cause of the carbon isotope excursion at the end of the Paleocene, *Paleoceanography*, *10*(6), 965–971, doi:10.1029/95PA02087.

Dickens, G. R., C. K. Paull, and P. Wallace (1997), Direct measurement of in situ methane quantities in a large gas-hydrate reservoir, *Nature*, *385*, 426–428, doi:10.1038/385426a0.

Flemings, P. B., X. Liu, and W. J. Winters (2003), Critical pressure and multiphase flow in Blake Ridge gas hydrates, *Geology*, *31*(12), 1057–1060, doi:10.1130/G19863.1.

Ginsburg, G. D., and V. A. Soloviev (1997), Methane migration within the submarine gas-hydrate stability zone under deep-water conditions, *Mar. Geol.*, *137*, 49–57, doi:10.1016/S0025-3227(96)00078-3.

Goldberg, D., T. Takahashi, and A. L. Slagle (2008), Carbon dioxide sequestration in deep-sea basalt, *Proc. Natl. Acad. Sci. U.S.A.*, *105*, 9920–9925, doi:10.1073/pnas.0804397105.

Gorman, A. R., W. S. Holbrook, M. J. Hornbach, K. L. Hackwith, D. Lizarralde, and I. Pecher (2002), Migration of methane gas through the hydrate stability zone in a low-flux hydrate province, *Geology*, *30*(4), 327–330, doi:10.1130/0091-7613(2002)030<0327:MOMGTT>2.0.CO;2.

Heeschen, K. U., A. M. Trehu, R. W. Collier, E. Suess, and G. Rehder (2003), Distribution and height of methane bubble plumes on the Cascadia Margin characterized by acoustic imaging, *Geophys. Res. Lett.*, *30*(12), 1643, doi:10.1029/2003GL016974.

Heeschen, K. U., R. W. Collier, M. A. de Angelis, E. Suess, G. Rehder, P. Linke, and G. P. Klinkhammer (2005), Methane sources, distributions, and fluxes from cold vent sites at Hydrate Ridge, Cascadia Margin, *Global Biogeochem. Cycles*, *19*, GB2016, doi:10.1029/2004GB002266.

Heeschen, K. U., H. J. Hohnberg, M. Haeckel, F. Abegg, M. Drews, and G. Bohrmann (2007), In situ hydrocarbon concentrations from pressurized cores in surface sediments, northern Gulf of Mexico, *Mar. Chem.*, *107*, 498–515, doi:10.1016/j.marchem.2007.08.008.

Holbrook, W. S., H. Hoskins, W. T. Wood, R. A. Stephen, and D. Lizarralde (1996), Methane hydrate and free gas on the Blake Ridge from vertical seismic profiling, *Science*, *273*, 1840–1842, doi:10.1126/science.273.5283.1840.

Hornbach, M. J., D. M. Saffer, and W. S. Holbrook (2004), Critically pressured free-gas reservoirs below gas-hydrate provinces, *Nature*, *427*(6970), 142–144, doi:10.1038/nature02172.

Hornbach, M. J., C. Ruppel, and C. L. V. Dover (2007), Three-dimensional structure of fluid conduits sustaining an active deep marine cold seep, *Geophys. Res. Lett.*, *34*, L05601, doi:10.1029/2006GL028859.

House, K. Z., D. P. Schrag, C. F. Harvey, and K. S. Lackner (2006), Permanent carbon dioxide storage in deep-sea sediments, *Proc. Natl. Acad. Sci. U.S.A.*, *103*, 12,291–12,295, doi:10.1073/pnas.0605318103.

Hovland, M., J. V. Gardner, and A. G. Judd (2002), The significance of pockmarks to understanding fluid flow processes and geohazards, *Geofluids*, *2*, 127–136, doi:10.1046/j.1468-8123.2002.00028.x.

Itasca Consulting Group, Inc. (Itasca) (2004), PFC2D, version 3.1, Theory and Background, Minneapolis, Minn.

Jain, A. K., and R. Juanes (2008), Pore-scale mechanistic study of the preferential mode of hydrate formation in sediments: Coupling of multiphase fluid flow and ediment mechanics, paper presented at 6th International Conference on Gas Hydrates, Vancouver, B. C., Canada.

Judd, A. G., M. Hovland, L. I. Dimitrov, S. Garcia Gil, and V. Jukes (2002), The geological methane budget at Continental Margins and its influence on climate change, *Geofluids*, *2*, 109–126, doi:10.1046/j.1468-8123.2002.00027.x.

Kato, S., T. Sakakibara, and H. Yoshimori (2004), Effects of intergranular adhesive force on behavior of granular material, in *Numerical Modeling in Micromechanics Via Particle Methods: Proceedings of the 2nd International PFC Symposium, Kyoto, Japan*, edited by Y. Shimizu, R. D. Hart, and P. Cundall, pp. 347–354, A. A. Balkema, Leiden, Netherlands.

Koide, H., M. Takahashi, and H. Tsukamoto (1995), Self-trapping mechanisms of carbon dioxide in the aquifer disposal, *Energy Convers. Manage.*, *36*, 505–508, doi:10.1016/0196-8904(95)00054-H.

Koide, H., Y. Shindo, Y. Tazaki, M. Iijima, K. Ito, N. Kimura, and K. Omata (1997a), Deep sub-seabed disposal of CO_2—The most protective storage, *Energy Convers. Manage.*, *38*, S253–S258, doi:10.1016/S0196-8904(96)00278-6.

Koide, H., M. Takahashi, Y. Shindo, Y. Tazaki, M. Iijima, K. Ito, N. Kimura, and K. Omata (1997b), Hydrate formation in sediments in the sub-seabed disposal of CO_2, *Energy*, *22*, 279–283, doi:10.1016/S0360-5442(96)00122-3.

Kvenvolden, K. A. (1988), Methane hydrate—A major reservoir of carbon in the shallow geosphere?, *Chem. Geol.*, *71*, 41–51, doi:10.1016/0009-2541(88)90104-0.

Lenormand, R., C. Zarcone, and A. Sarr (1983), Mechanisms of the displacement of one fluid by another in a network of capillary ducts, *J. Fluid Mech.*, *135*, 337–353, doi:10.1017/S0022112083003110.

Lenormand, R., E. Touboul, and C. Zarcone (1988), Numerical models and experiments on immiscible displacements in porous media, *J. Fluid Mech.*, *189*, 165–187, doi:10.1017/S0022112088000953.

Leverett, M. C. (1941), Capillary behavior of porous solids, *Petrol. Trans. AIME*, *142*, 152–169.

Levine, J. S., J. M. Matter, D. Goldberg, A. Cook, and K. S. Lackner (2007), Gravitational trapping of carbon dioxide in deep sea sediments: Permeability, buoyancy, and geomechanical analysis, *Geophys. Res. Lett.*, *34*, L24703, doi:10.1029/2007GL031560.

Li, L., and R. M. Holt (2001), Simulation of flow in sandstone with fluid coupled particle model, in *Rock Mechanics in the National Interest. Proceedings of the 38th U.S. Rock Mechanics Symposium, Washington, D.C.*, vol. 1, pp. 165–172, A. A. Balkema, Rotterdam, Netherlands.

Li, L., and R. M. Holt (2004), A study on the calculation of particle volumetric deformation in a fluid coupled PFC model, in *Numerical Modeling in Micromechanics Via Particle Methods. Proc. of the 2nd International PFC Symposium, Kyoto, Japan*, edited by Y. Shimizu, R. D. Hart, and P. Cundall, pp. 273–279, A. A. Balkema, Leiden, Netherlands.

Lian, G., C. Thornton, and M. J. Adams (1993), A theoretical study of the liquid bridge forces between two rigid spherical bodies, *J. Colloid Interface Sci.*, *161*, 138–147, doi:10.1006/jcis.1993.1452.

Liu, X., and P. B. Flemings (2006), Passing gas through the hydrate stability zone at southern Hydrate Ridge, offshore Oregon, *Earth Planet. Sci. Lett.*, *241*, 211–216, doi:10.1016/j.epsl.2005.10.026.

Liu, X., and P. B. Flemings (2007), Dynamic multiphase flow model of hydrate formation in marine sediments, *J. Geophys. Res.*, *112*, B03101, doi:10.1029/2005JB004227.

Mason, G., and N. R. Morrow (1991), Capillary behavior of a perfectly wetting liquid in irregular triangular tubes, *J. Colloid Interface Sci.*, *141*, 262–274, doi:10.1016/0021-9797(91)90321-X.

Mayer, R. P., and R. A. Stowe (1965), Mercury-porosimetry breakthrough pressure for penetration between packed spheres, *J. Colloid Interface Sci.*, *20*, 893.

Milkov, A. V., and W. Xu (2005), Comment on "Gas hydrate growth, methane transport, and chloride enrichment at the southern summit of Hydrate Ridge, Cascadia margin off Oregon" by Torres et al. [Earth Planet. Sci. Lett. 226:225–241 (2004)], *Earth Planet. Sci. Lett.*, *239*, 162–167, doi:10.1016/j.epsl.2005.05.044.

Milkov, A. V., et al. (2004), Co-existence of gas hydrate, free gas, and brine within the regional gas hydrate stability zone at Hydrate Ridge (Oregon margin): Evidence from prolonged degassing of a pressurized core, *Earth Planet. Sci. Lett.*, *222*, 829–843, doi:10.1016/j.epsl.2004.03.028.

Netzeband, G. L., C. P. Hübscher, D. Gajewski, J. W. G. Grobys, and J. Bialas (2005), Seismic velocities from the Yaquina forearc basin off Peru: Evidence for free gas within the gas hydrate stability zone, *Int. J. Earth Sci.*, *94*, 420–432, doi:10.1007/s00531-005-0483-2.

Nimblett, J., and C. Ruppel (2003), Permeability evolution during the formation of gas hydrates in marine sediments, *J. Geophys. Res.*, *108*(B9), 2420, doi:10.1029/2001JB001650.

Nunn, J. A., and P. Meulbroek (2002), Kilometer-scale upward migration of hydrocarbons in geopressured sediments by buoyancy-driven propagation of methane-filled fractures, *AAPG Bull.*, *86*(5), 907–918.

Obzhirov, A., R. Shakirov, A. Salyuk, E. Suess, N. Biebow, and A. Salomatin (2004), Relations between methane venting, geological structure and seismo-tectonics in the Okhotsk Sea, *Geo Mar. Lett.*, *24*, 135–139, doi:10.1007/s00367-004-0175-0.

Øren, P. E., S. Bakke, and O. J. Arntzen (1998), Extending predictive capabilities to network models, *Soc. Pet. Eng. J.*, *3*(4), 324–336.

Orr, F. M., L. E. Scriven, and A. P. Rivas (1975), Pendular rings between solids: Meniscus properties and capillary force, *J. Fluid Mech.*, *67*, 723–742, doi:10.1017/S0022112075000572.

Patzek, T. W. (2001), Verification of a complete pore network simulator of drainage and imbibition, *Soc. Pet. Eng. J.*, *6*(2), 144–156.

Patzek, T. W., and D. B. Silin (2001), Shape factor and hydraulic conductance in noncircular capillaries: I. One-phase creeping flow, *J. Colloid Interface Sci.*, *236*, 295–304, doi:10.1006/jcis.2000.7413.

Paull, C. K., P. G. Brewer, W. Ussler, E. T. Peltzer, G. Rehder, and D. Clague (2003), An experiment demonstrating that marine slumping is a mechanism to transfer methane from seafloor gas-hydrate deposits into the upper ocean and atmosphere, *Geo Mar. Lett.*, *22*, 198–203.

Potyondy, D. O., and P. A. Cundall (2004), A bonded-particle model for rock, *Int. J. Rock Mech. Min. Sci.*, *41*, 1329–1364, doi:10.1016/j.ijrmms.2004.09.011.

Princen, H. M. (1969a), Capillary phenomena in assemblies of parallel cylinders. I. Capillary rise between two cylinders, *J. Colloid Interface Sci.*, *30*, 69–75, doi:10.1016/0021-9797(69)90379-8.

Princen, H. M. (1969b), Capillary phenomena in assemblies of parallel cylinders. II. Capillary rise in systems with more than two cylinders, *J. Colloid Interface Sci.*, *30*, 359–371, doi:10.1016/0021-9797(69)90403-2.

Princen, H. M. (1970), Capillary phenomena in assemblies of parallel cylinders. III. Liquid columns between horizontal parallel cylinders, *J. Colloid Interface Sci.*, *34*, 171–184, doi:10.1016/0021-9797(70)90167-0.

Prodanovic, M., and S. Bryant (2006), A level set method for determining critical curvatures for drainage and imbibition, *J. Colloid Interface Sci.*, *304*, 442–458.

Richards, L. A. (1931), Capillary conduction of liquids through porous mediums, *Physics*, *1*, 318–333, doi:10.1063/1.1745010.

Riedel, M., T. S. Collett, M. J. Malone, and the Expedition 311 Scientists (Eds.) (2006), *Cascadia Margin Gas Hydrates, Proc. IODP, Expedition Reports*, vol. 311, Integrated Ocean Drilling Program, College Station, Tex.

Ruppel, C., G. R. Dickens, D. G. Castellini, W. Gilhooly, and D. Lizarralde (2005), Heat and salt inhibition of gas hydrate formation in the northern Gulf of Mexico, *Geophys. Res. Lett.*, *32*, L04605, doi:10.1029/2004GL021909.

Sahling, H., G. Bohrmann, V. Spiess, J. Bialas, M. Breitzke, M. Ivanov, S. Kasten, S. Krastel, and R. Schneider (2008), Pockmarks in the Northern Congo Fan area, SW Africa: Complex seafloor features shaped by fluid flow, *Mar. Geol.*, *249*, 206–225, doi:10.1016/j.margeo.2007.11.010.

Sassen, R., S. L. Losh, L. Cathles III, H. H. Roberts, J. K. Whelan, A. V. Milkov, S. T. Sweet, and D. A. DeFreitas (2001), Massive vein-filling gas hydrate: Relation to ongoing gas migration from the deep subsurface in the Gulf of Mexico, *Mar. Pet. Geol.*, *18*, 551–560, doi:10.1016/S0264-8172(01)00014-9.

Shimizu, Y. (2004), Fluid coupling in PFC2D and PFC3D, in *Numerical Modeling in Micromechanics Via Particle Methods. Proc. of the 2nd International PFC Symposium, Kyoto, Japan*, edited by Y. Shimizu, R. D. Hart, and P. Cundall, pp. 281–287, A. A. Balkema, Leiden, Netherlands.

Sloan, E. D. (1998), *Clathrate Hydrates of Natural Gases*, 2nd ed., Marcel Deker, New York.

Sloan, E. D. (2003), Fundamental principles and applications of natural gas hydrates, *Nature*, *426*, 353–359, doi:10.1038/nature02135.

Soloviev, V. A., and G. D. Ginsburg (1997), Water segregation in the course of gas hydrate formation and accumulation in submarine gas-seepage fields, *Mar. Geol.*, *137*, 59–68, doi:10.1016/S0025-3227(96)00079-5.

Suess, E., et al. (1999), Gas hydrate destabilization: enhanced dewatering, benthic material turnover and large methane plumes at the Cascadia convergent margin, *Earth Planet. Sci. Lett.*, *170*, 1–15, doi:10.1016/S0012-821X(99)00092-8.

Tan, B. B. (2004), Geotechnical characterization of sediments from Hydrate Ridge, Cascadia continental margin, M.Sc. thesis, Mass. Inst. of Technol., Cambridge.

Tan, B. B., J. T. Germaine, and P. B. Flemings (2006), Data report: Consolidation and strength characteristics of sediments from ODP Site 1244, Hydrate Ridge, Cascadia continental margin, *Proc. Ocean Drill. Program Sci.*, *204*.

Terzaghi, K. (1943), *Theoretical Soil Mechanics*, John Wiley, New York.

Torres, M. E., J. McManus, D. E. Hammond, M. A. de Angelis, K. U. Heeschen, S. L. Colbert, M. D. Tryon, K. M. Brown, and E. Suess (2002), Fluid and chemical fluxes in and out of sediments hosting methane hydrate deposits on Hydrate Ridge, OR, I: Hydrological provinces, *Earth Planet. Sci. Lett.*, *201*, 525–540, doi:10.1016/j.epsl.2004.07.029.

Torres, M. E., K. Wallman, A. M. Trehu, G. Bohrmann, W. S. Borowski, and H. Tomaru (2004), Gas hydrate growth, methane transport, and chloride enrichment at the southern summit of Hydrate Ridge, Cascadia margin off Oregon, *Earth Planet. Sci. Lett.*, *226*, 225–241, doi:10.1016/j.epsl.2004.07.029.

Torres, M. E., K. Wallman, A. M. Trehu, G. Bohrmann, W. S. Borowski, and H. Tomaru (2005), Reply to comment on: "Gas hydrate growth, methane transport, and chloride enrichment at the southern summit of Hydrate Ridge, Cascadia margin off Oregon", *Earth Planet. Sci. Lett.*, *239*, 168–175, doi:10.1016/j.epsl.2005.08.012.

Trehu, A. M., et al. (2004a), Feeding methane vents and gas hydrate deposits at south Hydrate Ridge, *Geophys. Res. Lett.*, *31*, L23310, doi:10.1029/2004GL021286.

Trehu, A. M., et al. (2004b), Three-dimensional distribution of gas hydrate beneath southern Hydrate Ridge: constraints from ODP Leg 204, *Earth Planet. Sci. Lett.*, *222*, 845–862, doi:10.1130/0091-7613(1999)027<1075:MOTADF>2.3.CO;2.

Trehu, A. M., , G. Bohrmann, M. E. Torres, and F. S. Colwell (Eds.) (2006a), Drilling gas Hhydrates on Hydrate Ridge, Cascadia Continental Margin, *Proc. Ocean Drill. Program Sci. Results*, *204*, doi:10.2973/odp.proc.sr.204.2006.

Trehu, A. M., C. Ruppel, M. Holland, G. R. Dickens, M. E. Torres, T. S. Collett, D. Goldberg, R. Riedel, and P. Schultheiss (2006b), Gas hydrates in marine sediments: Lessons from scientific drilling, *Oceanography*, *19*(4), 124–143.

Tryon, M. D., K. M. Brown, M. E. Torres, A. M. Trehu, J. McManus, and R. W. Collier (1999), Measurements of transience and downward fluid flow near episodic methane gas vents, Hydrate Ridge, Cascadia, *Geology*, *27*(12), 1075–1078, doi:10.1130/0091-7613(1999)027<1075:MOTADF>2.3.CO;2.

Tryon, M. D., K. M. Brown, and M. E. Torres (2002), Fluid and chemical flux in and out of sediments hosting methane hydrate deposits on Hydrate Ridge, OR, II: Hydrological processes, *Earth Planet. Sci. Lett.*, *201*, 541–557, doi:10.1016/S0012-821X(02)00732-X.

Waite, W. F., T. J. Kneafsey, W. J. Winters, and D. H. Mason (2008), Physical property changes in hydrate-bearing sediment due to depressurization and subsequent repressurization, *J. Geophys. Res.*, *113*, B07102, doi:10.1029/2007JB005351.

Wang, H. F. (2000), *Theory of Linear Poroelasticity*, Princeton Univ. Press, Princeton, N. J.

Weinberger, J. L., and K. M. Brown (2006), Fracture networks and hydrate distribution at Hydrate Ridge, Oregon, *Earth Planet. Sci. Lett.*, *245*, 123–136, doi:10.1016/j.epsl.2006.03.012.

Weinberger, J. L., K. M. Brown, and P. E. Long (2005), Painting a picture of gas hydrate distribution with thermal images, *Geophys. Res. Lett.*, *32*, L04609, doi:10.1029/2004GL021437.

Wilkinson, D., and J. Willemsen (1983), Invasion percolation: A new form of percolation theory, *J. Phys. A*, *16*, 3365–3376, doi:10.1088/0305-4470/16/14/028.

Wood, W. T., J. F. Gettrust, N. R. Chapman, G. D. Spence, and R. D. Hyndman (2002), Decreased stability of methane hydrates in marine sediments owing to phase-boundary roughness, *Nature*, *420*, 656–660, doi:10.1038/nature01263.

Zühlsdorff, L., and V. Spiess (2004), Three-dimensional seismic characterization of a venting site reveals compelling indications of natural hydraulic fracturing, *Geology*, *32*(2), 101–104, doi:10.1130/G19993.1.

───────────────

R. Juanes (corresponding author) and A. K. Jain, Department of Civil and Environmental Engineering, Massachusetts Institute of Technology, 77 Massachusetts Avenue, Building 48-319, Cambridge, MA 02139, USA. (juanes@mit.edu)